*J. Fluid Mech.* (2012), *vol.* 699, *pp.* 115–152. © Cambridge University Press 2012 
doi:10.1017/jfm.2012.86

# On the response of convectively unstable flows to oscillatory forcing with application to liquid sheets

**N. S. Barlow[1]†, S. J. Weinstein[2] and B. T. Helenbrook[3]**

[1] Department of Chemical and Biological Engineering, University at Buffalo, State University of New York, Buffalo, NY 14260, USA

[2] Department of Chemical and Biomedical Engineering, Rochester Institute of Technology, Rochester, NY 14623, USA

[3] Department of Mechanical and Aeronautical Engineering, Clarkson University, Potsdam, NY 13699, USA

(Received 1 June 2011; revised 20 November 2011; accepted 9 February 2012; first published online 19 April 2012)

The complete integral solution is found for the convectively unstable and oscillatory-forced linear Klein–Gordon equation as a function of spatial variable, $x$, and time, $t$. A comparison of the integral solution with series solutions of the Klein–Gordon equation elucidates salient features of both the transient and long-time spatially growing solutions. A rigorous method is developed for identifying the key $x/t$ rays associated with saddle points that can be used to characterize the transition between transient temporally growing and long-term spatially growing waves. This method effectively combines the procedure given by Gordillo & Pérez-Saborid (*Phys. Fluids*, vol. 14, 2002, pp. 4329–4343) for determining the $x/t$ ray at which the forced spatial growth response affects the observed waveform and competes with the transient response, with an established methodology for identifying the leading and trailing edge rays of an impulse response. The method is applied to a linearized system describing an oscillatory-forced liquid sheet and asymptotic predictions are obtained. Series solutions are used to validate these predictions. We establish that the portion of the solution responsible for spatial growth in the signalling problem is correctly identified by Gordillo & Pérez-Saborid (*Phys. Fluids*, vol. 14, 2002, pp. 4329–4343), and that this interpretation is in contrast with the classical literature. The approach provided here can be applied in multiple ways to study a convectively unstable oscillatory-forced medium. In cases where numerical or series solutions are readily available, the proposed method is used to extract key features of the solution. In cases where only the forced long time behaviour is needed, the dispersion relation is used to extract: (i) the time required to see the forced solution; (ii) the amplitude, phase and spatial growth of the forced solution; and (iii) the breadth of the transient.

**Key words:** absolute/convective instability, instability control, thin films

## 1. Introduction

The response of a potentially unstable medium to an oscillating point or line source is known as ‘signalling’. In the context of a one-dimensional propagation problem,

† Email address for correspondence: barlow.nate@gmail.com

https://doi.org/10.1017/jfm.2012.86 Published online by Cambridge University Press

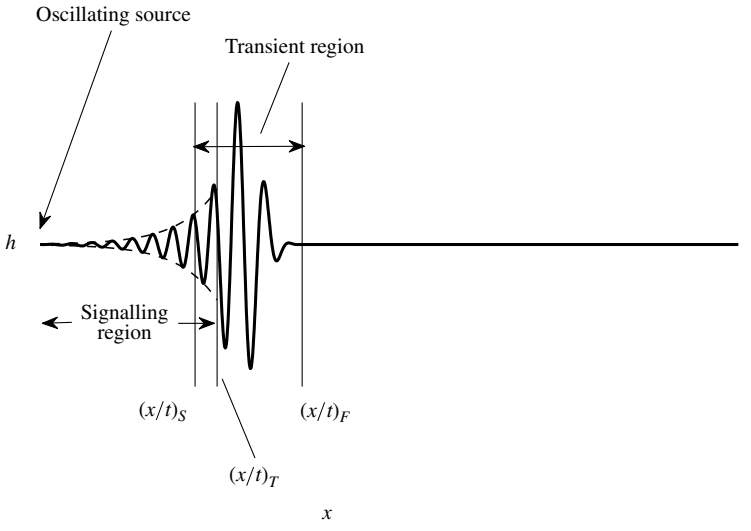



FIGURE 1. A schematic of signalling behaviour at a fixed time. Key regions of the response are delimited by $x/t$ rays that move downstream with the wave packet.

this corresponds to the response induced by a forcing term $f(x,t) = A\delta(x)\mathrm{e}^{-\mathrm{i}\omega_f t}$ where $\omega_f$ is the forcing frequency, $A$ is the forcing amplitude, $x$ is the coordinate along the medium and $\delta$ is the Dirac delta function. The response to such forcing is directly applicable to liquid sheets, particularly in the context of thin locally uniform film formation used in coating flows (Weinstein & Ruschak 2004). As shown in Clarke *et al.* (1997) and Weinstein *et al.* (1997), a pressure disturbance in the surrounding air can lead to undesirable deformations of liquid sheets (curtains) in the process of curtain coating. To better understand the stability of forced mediums in general, a small subset of problems termed 'signalling problems' have appeared in the spatio-temporal stability literature over the past three decades.

Bers (1983) studied the signalling problem applied to convectively unstable waves and discussed the competition between a temporally growing transient and a temporally stable yet spatially growing oscillatory response downstream of the forcing. Bers correctly concluded that the spatial growth is directly related to poles in the Fourier integral solution, but attributed the spatial growth to a residue contribution that, in fact, spatially decays (see § 2.2). A similar interpretation is given in Huerre (1987, 2000) and Huerre & Monkewitz (1990). Gordillo & Pérez-Saborid (2002) identified the correct integral responsible for spatial growth and, through analysis, introduced the idea of a 'limiting ray' $x/t$ that determines the space–time ratio below which the magnitude of the spatially growing response and the transient response are comparable.

A schematic of signalling behaviour is shown in figure 1, where wave amplitude $h$ is plotted against $x$ for a fixed time. In the figure, key regions of the response are delimited by $x/t$ rays that move downstream with the wave packet. The limiting ray of Gordillo & Pérez-Saborid (2002) is labelled $(x/t)_T$, beyond which the total response is dominated by the transient. The rays $(x/t)_S$ and $(x/t)_F$ indicate the breadth of the transient. These rays are identified using the criteria given in Gaster (1968) (see § 2.3) and are denoted respectively as $V_-$ and $V_+$ in Huerre (2000) for a non-oscillatory 'impulse response', where the forcing is given by $A\delta(x)\delta(t)$. The rays $(x/t)_S$ and $(x/t)_F$,

https://doi.org/10.1017/jfm.2012.86 Published online by Cambridge University Press

respectively, define the trailing and leading edges of the temporally growing wave packet. The interpretation of these rays in Gaster (1968), Monkewitz (1990) and Huerre (2000) is identical to that given here for the oscillatory-forced problem, with one exception. For the impulse response, the flow is calm upstream of the ray $(x/t)_S$ $(V_-)$. However, in an oscillatory-forced medium, the flow can exhibit downstream spatial amplification in this region, as shown in figure 1. The 'signalling region' labelled in figure 1 indicates the region of flow that is affected by varying the input forcing frequency, $\omega_f$, and forcing amplitude, $A$. A complete description of these rays and regions is provided in this paper.

The objective of this work is to construct long-time asymptotic predictions for each region of figure 1, and to provide an exact solution for the spatially growing oscillatory response, both of which can be used to interpret an existing numerical or series solution. Using the dispersion relation alone, we develop a method for extracting certain $x/t$ rays that characterize the response of the system. The ray $(x/t)_S$, indicated in figure 1, is inherently important, as it provides the time beyond which the transient response has moved out of a given region; beyond this time, the system resides in the purely spatial growth regime (i.e. the signalling region of figure 1), where the response is controllable by varying the amplitude and frequency of the forcing. Our method leads to an exact solution for this regime, which explicitly gives the amplitude and frequency of the induced wave response as a function of the amplitude and frequency of an input disturbance. This transfer function has practical utility, as the source of the induced response can often be isolated and controlled in a process.

The paper is organized as follows. In § 2, we solve the oscillatory-forced linear Klein–Gordon equation in order to develop the asymptotic technique. In § 2.1, the equation is solved via a series solution, and both temporal and spatial stability analyses are used to interpret the simulated wave dynamics. In § 2.2, we find the asymptotic behaviour of the integral solution and identify errors in the previous literature. In this section, we provide a complete spatio-temporal description of convectively unstable flow for the oscillatory-forced linear Klein–Gordon equation. This leads to a procedure, described in § 2.3, for extracting the key $x/t$ rays that characterize both the transient and continually forced solution in a convectively unstable system. To illustrate the generality of the method, we apply the analysis to a planar liquid sheet. A description of the physical model, governing equations and boundary conditions for a forced liquid sheet is given in § 3.1. The integral and series solutions of a linearized system describing the forced sheet are also given in this section. In § 3.2, we evaluate the series solution for sinuous and varicose waves in a sheet and compare the behaviour with asymptotic predictions obtained through the procedure described in § 2.3.

## 2. Signalling in the Klein–Gordon equation

With the goal of developing a general procedure for extracting the important features of spatially developing forced flows, we start with a tractable model problem: the forced linear Klein–Gordon equation. We wish to find the response to an oscillating line source located at $x = 0$ in an infinite medium, where the wave height $h(x, t)$ is governed by

$$\left.\begin{aligned} \left(\frac{\partial}{\partial t} + U\frac{\partial}{\partial x}\right)^2 h - \frac{\partial^2 h}{\partial x^2} - \mu h &= A\delta(x)\mathrm{e}^{-\mathrm{i}\omega_f t}, \quad t \geqslant 0, \\ h(x,0) &= \frac{\partial h}{\partial t}(x,0) = 0 \quad \text{for all } x \end{aligned}\right\} \tag{2.1}$$

https://doi.org/10.1017/jfm.2012.86 Published online by Cambridge University Press

where $U$ and $\mu$ are real parameters and $h(x,t)=0$ for $t<0$. These parameters ultimately affect wave dynamics, but otherwise are not linked to any particular physical properties; (2.1) is considered dimensionless in this exercise. The unforced Klein–Gordon equation subject to an initial disturbance has been studied extensively by Huerre (1987); therefore, we only focus on the forced response of an initially undisturbed medium. Huerre showed that the problem is stable for $\mu<0$, absolutely unstable when $\mu>0$ and $|U|<1$ and convectively unstable for

$$\mu>0 \quad \text{and} \quad |U|>1. \tag{2.2}$$

The analyses herein assume the constraints given in (2.2), since we are only interested in convective instability. In an absolutely unstable medium, an initial disturbance grows and eventually contaminates the entire domain, causing continued forcing to become subdominant and inconsequential as $t\to\infty$. In this limit, the absolutely unstable forced case is equivalent to the unforced case studied by Huerre (1987). Equation (2.1) is hyperbolic, and its characteristic velocities are given by $\mathrm{d}x/\mathrm{d}t=U\pm1$. This indicates that convectively unstable waves either travel completely downstream ($U>1$) or completely upstream ($U<-1$). Regardless of direction, the foregoing analysis of growth and propagation is identical. To organize ideas, we limit our discussion to waves that convect and grow downstream ($x>0$) of the source by choosing $U>1$.

### 2.1. *Series solution and basic stability analysis*

The solution of (2.1) on either a finite or infinite domain can be thought of as a superposition of modes, each given by

$$h_k(x,t)=C_k\mathrm{e}^{\mathrm{i}(kx-\omega t)}, \tag{2.3}$$

where $C_k$ is the amplitude associated with a particular mode, $k=k_r+\mathrm{i}k_i$ is the possibly complex wavenumber, and $\omega=\omega_r+\mathrm{i}\omega_i$ is the possibly complex wave frequency. The relationship between the wavenumber and wave frequency for a given medium is obtained by substituting (2.3) into the homogenous version of the constant coefficient linear partial differential equation of interest. This transforms the differential equation in $h(x,t)$ into the algebraic equation, $D(k,\omega)=0$, which is referred to as the dispersion relation. Substituting (2.3) into (2.1) (neglecting initial conditions) with $A=0$ leads to

$$D(\omega,k)=-(\omega-Uk)^2+k^2-\mu \tag{2.4}$$

where $D(\omega,k)=0$ describes the relationship between $k$ and $\omega$ in the Klein–Gordon equation.

#### 2.1.1. *Series solution*

To validate the following stability analysis, we use the Fourier series solution of (2.1) for periodic boundary conditions $h(-L,t)=h(L,t)$, given by

$$h(x,t)=\frac{A}{2L}\times\sum_{n=-N}^{n=N}\frac{\left[\cosh\left(\frac{\Delta_n}{2}t\right)+(2U\mathrm{i}k_n-2\mathrm{i}\omega_f)\sinh\left(\frac{\Delta_n}{2}t\right)\Big/\Delta_n\right]\mathrm{e}^{-t/2}-\mathrm{e}^{-\mathrm{i}\omega_f t}}{D(k_n,\mathrm{i}\omega_f)}\mathrm{e}^{\mathrm{i}k_n x} \tag{2.5}$$

where $\Delta_n=2\sqrt{\mu+(1-2U^2)k_n^2}$, $k_n=n\pi/L$, and $D(k_n,\mathrm{i}\omega_f)$ is obtained using (2.4). The series solution (2.5) is constructed using real wavenumbers $k_n$. Note that we could

https://doi.org/10.1017/jfm.2012.86 Published online by Cambridge University Press

have also constructed the same solution using complex wavenumbers, as outlined in Barlow *et al.* (2010). Solutions are valid provided that the leading edge of the downstream response does not reach the boundaries of the domain at $x = \pm L$. For the figures and comparisons to follow, we use a domain length of $L = 200$, take 401 terms in the series ($N = 200$) and use parameter values of $\mu = 1$ and $U = 2$.

2.1.2. *Stability analysis*

If we assume that the dominant spatial or temporal growth is exponential in form, the maximum growth rates can be inferred from (2.3) by applying $D(\omega, k) = 0$ in (2.4). In classical temporal analysis, the maximum temporal growth rate is given by the largest positive value of $\omega_i$ for a real-valued wavenumber $k_r$. Conversely, the spatial growth rate associated with a particular real-valued forcing frequency $\omega_f$ is given by the largest negative value of $k_i$ for waves moving in the $x > 0$ direction. Waves studied in this analysis travel downstream only. However, the ideas developed herein also apply to waves that travel upstream away from the source, except the spatial growth rate would then be given by the most positive value of $k_i$ for a particular $\omega_f$. The $D(k, \omega) = 0$ solutions of $\omega$ and $k$ in (2.4) are given respectively by

$$\omega^{\pm}(k) = Uk \pm \sqrt{k^2 - \mu} \tag{2.6}$$

and

$$k_{f1,f2} = -\frac{\omega_f U}{1 - U^2} \pm \frac{1}{1 - U^2}\sqrt{\omega_f^2 + \mu(1 - U^2)} \tag{2.7}$$

where $k_{f1}$ and $k_{f2}$ are the respective $+$ and $-$ roots associated with real-valued frequencies $\omega = \omega_f$. A temporal amplification plot is given in figure 2, where the imaginary part of (2.6) is plotted versus real $k$. Since $\omega_i|_{k=0} = \sqrt{\mu}$ is a maximum in figure 2, the group velocity $\partial\omega/\partial k = \partial\omega_r/\partial k_r + \mathrm{i}(\partial\omega_i/\partial k_r)$ takes on a real value, and $\partial\omega/\partial k|_{k=0} = U$ specifies the speed at which the peak of the transient wave packet travels away from the source, growing like $\mathrm{e}^{\sqrt{\mu}t}$. This unique real-valued mode (where $\partial\omega_i/\partial k_r = 0,\ \omega_i > 0$) can be used to describe the motion of the transient solution to (2.1). This can be seen in figure 3, where the series solution is plotted for $\mu = 1,\ U = 2,\ \omega_f = 1.632$. The peak of the transient moves exactly $x = Ut$ units away from the source; the Gaussian-like waveform results from the culmination of both slower and faster moving waves, which also grow exponentially with smaller growth rates than the maximum. After the transient has passed a certain region, an oscillatory-forced spatially growing region (a tail) is left behind. The solution is shown at a later time ($t = 40$) in figure 4, where both the Gaussian-like transient (figure 4*a*) and the spatially growing tail (figure 4*c*) are clearly observed. Here, the transient has moved exactly $x = Ut = 80$ units away from the source and grows like $\mathrm{e}^{\sqrt{\mu}t}$ as $t \to \infty$; this is shown in figure 4(*b*) where the maximum amplitude of the series solution is plotted against time.

The variation of spatial growth rate with forcing frequency is given in the bottom half-plane of figure 5, provided $x > 0$. The frequency range that allows for $x > 0$ spatial growth ($k_i < 0$) is $\omega_f^2 < |\mu(1 - U^2)|$. Forcing in this range is a necessary but not sufficient condition to have spatially growing waves. We will show in § 2.2 that it is also necessary for temporally unstable saddle points to exist in the dispersion relation (2.4), ensuring that a growing transient leads the spatially growing waves. For the parameters chosen, $\omega_f = 1.6321$ falls within the range of potential spatial instability. The spatial growth rate is given by $\mathrm{Im}(k_{f1}) = -0.1933$ from (2.7), which is consistent with a region that follows the transient and grows like $\approx \mathrm{e}^{-\mathrm{Im}(k_{f1})x}$, shown in

https://doi.org/10.1017/jfm.2012.86 Published online by Cambridge University Press

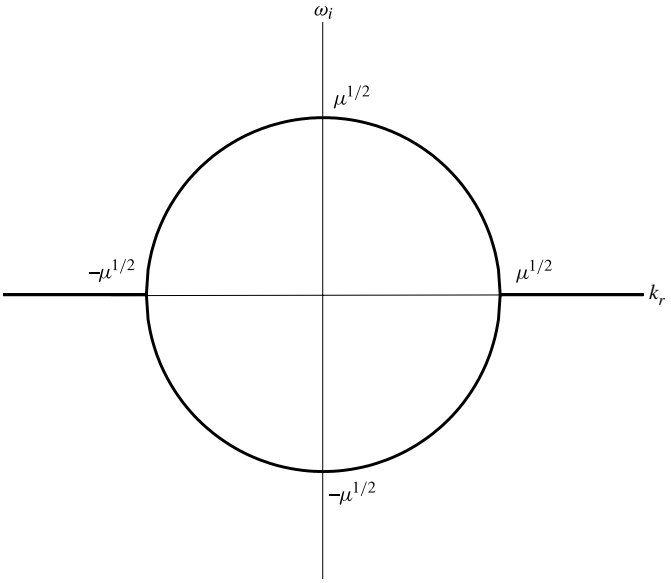



FIGURE 2. Temporal amplification plot of the Klein–Gordon equation; $\omega(k)$ is given by (2.6).

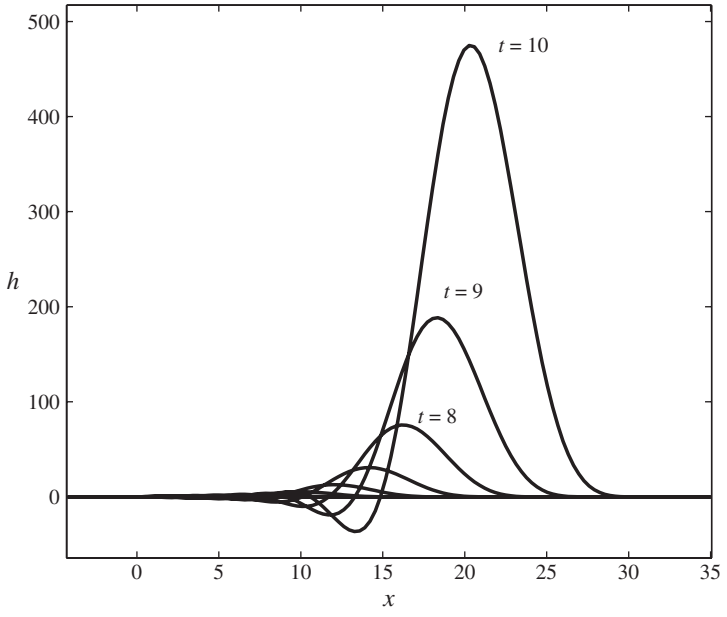



FIGURE 3. Convectively unstable evolution of the forced Klein–Gordon equation (2.1). The series solution is given by (2.5) with $\mu = 1$, $U = 2$ and $\omega_f = 1.632$. On the scale of the transient response, the influence of the sinusoidal forcing is not clearly seen in this figure. Figure 4(*c*) provides a close-up of the spatially growing region that precedes the transient response.

figure 4(*c*). This can be considered a steady spatially growing envelope and a solution of (2.1) within a certain distance from the source, since the wave envelope remains at the same amplitude for all time at a given location, although the phase varies as

https://doi.org/10.1017/jfm.2012.86 Published online by Cambridge University Press

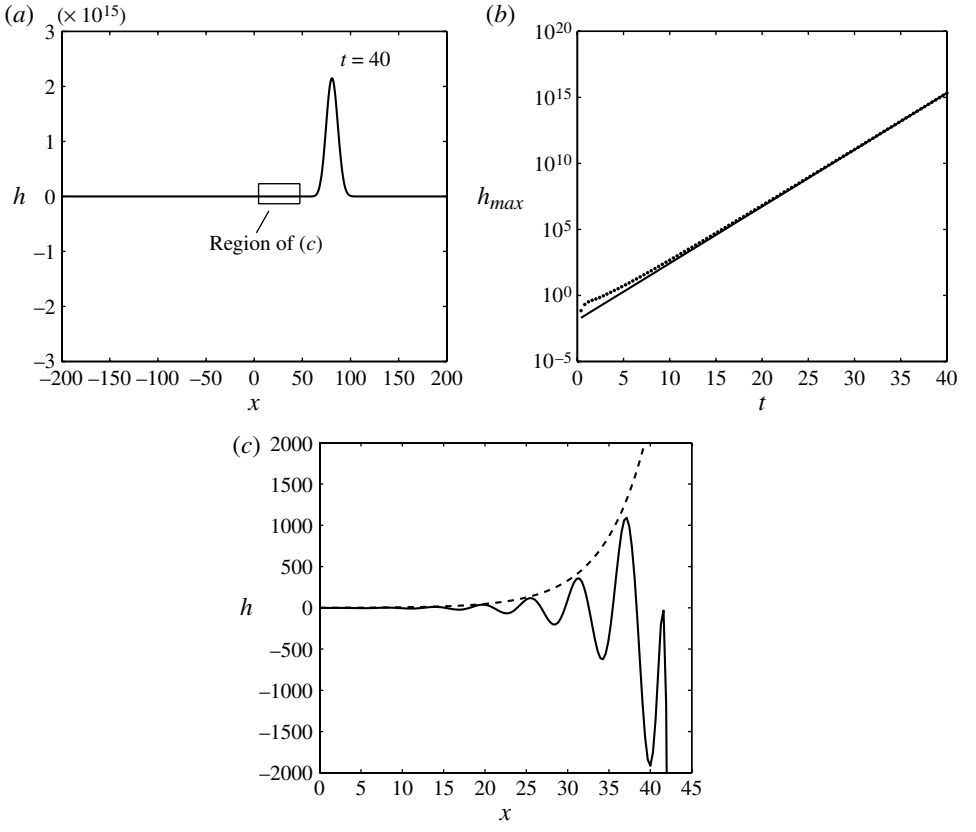



FIGURE 4. Series solution of (2.1) with $\mu = 1$, $U = 2$ and $\omega_f = 1.632$. (*a*) Full domain of the solution at $t = 40$. (*b*) Maximum growth of the solution (•) compared with the curve $Ae^{\sqrt{\mu}t}$ (——). (*c*) Magnification of the solution at $t = 40$, showing the steady spatially growing envelope, which aligns with the curve $Ae^{-\mathrm{Im}(k_{f1})x}$ (– –), where $\mathrm{Im}(k_{f1}) = -0.1933$ from (2.7).

the system is continually forced. Note that the other root ($k_{f2}$) predicts spatial growth upstream ($x < 0$) of the source with a spatial growth rate given by $\mathrm{Im}(k_{f2}) = 0.1933$. In the following section, we show that only downstream spatial growth is relevant for $U > 1$.

The classical stability analysis provides us with a qualitative yet incomplete description of the solution, as it cannot be used to sufficiently anticipate the Fourier series results. We now continue to extract the key features of the series solution by examining the spatio-temporal behaviour of the relevant integral equations governing the system. We will find that this evaluation leads to a quantitative description of the flow.

### 2.2. *Integral solution*

To obtain the double integral solution of a constant coefficient linear partial differential equation, the Fourier and Laplace transforms are taken, the transformed dependent variable is then solved for and successive inverse transforms are taken to return to the original variable; detailed examples are given in Barlow *et al.* (2010) for similar wave evolution equations. Following this procedure, the integral solution

https://doi.org/10.1017/jfm.2012.86 Published online by Cambridge University Press

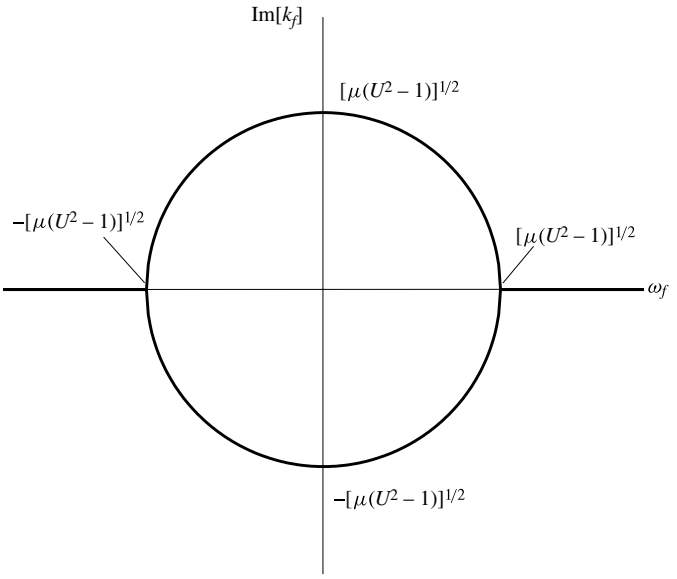



FIGURE 5. Spatial amplification plot of the Klein–Gordon equation; $k_f(\omega_f)$ is given by (2.7).

to (2.1) is

$$h(x,t) = \frac{1}{4\pi^2}\int_{-\infty}^{\infty}\int_{-\infty+i\tau_0}^{\infty+i\tau_0} \frac{A\mathrm{i}\,\mathrm{e}^{\mathrm{i}(kx-\omega t)}}{(\omega-\omega_f)D(k,\omega)}\,\mathrm{d}\omega\,\mathrm{d}k \tag{2.8}$$

where the parameter $\tau_0$ is taken such that the horizontal integration path in the $\omega_r - \omega_i$ plane passes above all singularities in the integrand; this comes from the definition of the inverse Laplace transform (Morse & Feshbach 1953). In addition, the path of the Fourier inversion is along the real axis in (2.8). For simple $\omega$ poles, the inner (Laplace) integral of (2.8) can be evaluated first by the method of residues, leaving us with the Fourier integral solution,

$$\begin{aligned} h(x,t) = {} & \overbrace{\frac{A}{2\pi}\int_{-\infty}^{\infty} \frac{\mathrm{e}^{\mathrm{i}[kx-\omega^+(k)t]}}{[\omega^+(k)-\omega_f]\dfrac{\partial D}{\partial\omega}[k,\omega^+(k)]}\,\mathrm{d}k}^{h_A^+(x,t)} \\ & + \overbrace{\frac{A}{2\pi}\int_{-\infty}^{\infty} \frac{\mathrm{e}^{\mathrm{i}[kx-\omega^-(k)t]}}{[\omega^-(k)-\omega_f]\dfrac{\partial D}{\partial\omega}[k,\omega^-(k)]}\,\mathrm{d}k}^{h_A^-(x,t)} \\ & + \underbrace{A\frac{\mathrm{e}^{-\mathrm{i}\omega_f t}}{2\pi}\int_{-\infty}^{\infty}\frac{\mathrm{e}^{\mathrm{i}kx}}{D(k,\omega_f)}\,\mathrm{d}k}_{h_B(x,t)} \end{aligned} \tag{2.9}$$

where $\partial \mathrm{D}/\partial\omega[k,\omega^{\pm}(k)] = \mp 2\sqrt{k^2-\mu}$, revealing branch point singularities $k = \pm\sqrt{\mu}$. When complex contour integration is used, the poles of all integrals in (2.9) are given

https://doi.org/10.1017/jfm.2012.86 Published online by Cambridge University Press

by (2.7); in $h_A^+(x,t)$ of (2.9), the pole $k_{f1}$ satisfies $\omega^+(k)-\omega_f=0$; in $h_A^-(x,t)$ of (2.9), the pole $k_{f2}$ satisfies $\omega^-(k)-\omega_f=0$.

When contour integration is used to evaluate $h_B(x,t)$ of (2.9), the poles $k_{f1}$ and $k_{f2}$ both satisfy $D(k,\omega_f)=0$. This integral can easily be evaluated by taking the residue with respect to $k$. Depending on the sign of $x$, the integration path is closed by a semicircle in either the upper or lower half of the $k_r$–$k_i$ plane. The real part of the exponential argument along this deformed contour must be negative as $k\to\pm\infty$, to ensure convergence. After the residue of $h_B(x,t)$ is evaluated and the expression for $\partial D/\partial\omega[k,\omega^{\pm}(k)]$ is inserted into $h_A^+(x,t)$ and $h_A^-(x,t)$, (2.9) becomes

$$h(x,t)=h_A^+ + h_A^- + h_B \tag{2.10}$$

where

$$h_A^+(x,t)+h_A^-(x,t)=\frac{A}{2\pi}\int_{-\infty}^{\infty}\frac{\mathrm{e}^{\mathrm{i}[kx-\omega^+(k)t]}}{-2\sqrt{k^2-\mu}[\omega^+(k)-\omega_f]}\,\mathrm{d}k + \frac{A}{2\pi}\int_{-\infty}^{\infty}\frac{\mathrm{e}^{\mathrm{i}[kx-\omega^-(k)t]}}{2\sqrt{k^2-\mu}[\omega^-(k)-\omega_f]}\,\mathrm{d}k \tag{2.11}$$

and

$$h_B(x,t)=A\mathrm{i}\mathrm{e}^{-\mathrm{i}\omega_f t}\left[H(x)\frac{\mathrm{e}^{\mathrm{i}k_{f2}x}}{\dfrac{\partial D}{\partial k}(k_{f2},\omega_f)}-H(-x)\frac{\mathrm{e}^{\mathrm{i}k_{f1}x}}{\dfrac{\partial D}{\partial k}(k_{f1},\omega_f)}\right]. \tag{2.12}$$

In (2.12), $H$ is the Heaviside step function used to combine the evaluation of the integral $h_B$ (in (2.9)) when $x>0$ and when $x<0$. For this problem, $k_{f2}$ is enclosed in the upper half ($x>0$) $k$-plane and $k_{f1}$ is enclosed in the lower half ($x<0$) $k$-plane. Consequently, $h_B$ is neutral in time and represents a spatially decaying waveform determined by the forcing frequency, $\omega_f$. It is important to point out that, even when forced at an 'unstable' forcing frequency ($\omega_f^2<|\mu(1-U^2)|$), $h_B$ cannot be responsible for spatial growth, as the step functions that arise to assure convergence preclude such growth.

In Bers (1983), Huerre (1987, 2000), Huerre & Monkewitz (1990) and possibly other publications, spatial growth is incorrectly attributed to $h_B$. In these publications, the double integral (2.8) is evaluated in the same order as above, with the $\omega$ integration performed first, leading to a $k$ integral given by (2.9). Also, in each of these publications, the $\omega$ path of integration is originally taken to be above all singularities in the $\omega_i$–$\omega_r$-plane and the $k$ path of integration is originally taken along the $k_r$-axis; these are also the paths used here. Note, that the Fourier inversion integral can also be taken anywhere in the strip of absolute convergence (i.e. strip of analyticity) in the complex $k$-plane, defined by $\mathrm{Im}(\epsilon_1)<k_i<\mathrm{Im}(\epsilon_2)$, where $\epsilon_1$ and $\epsilon_2$ are the closest singularities (of the integrand) respectively below and above the $k_r$-axis (Morse & Feshbach 1953). The necessary inclusion of the $k_r$-axis within this strip is central to the argument that $h_B$ is evaluated incorrectly in the literature. This inclusion comes from the classical derivation of a Fourier transform, which starts with a discrete Fourier series that arises from a self-adjoint eigenvalue problem on a finite domain. By definition these eigenvalues are real. The transform arises in the limit of the domain becoming infinite in extent. The eigenvalues congeal into a continuous spectrum, corresponding to the locus of real-valued wavenumbers ($k_r$) in the complex $k$-plane (Morse & Feshbach 1953; Lighthill 1962). Cauchy's theorem then allows one

https://doi.org/10.1017/jfm.2012.86 Published online by Cambridge University Press

to use any path that lies within the strip of absolute convergence to evaluate the Fourier inversion integral (Morse & Feshbach 1953; Bers 1983).

When evaluating the Fourier inversion integral of (2.8), Huerre (2000) reasoned that the $k$-integration path can be moved below a fixed $k_f$ pole that lies below the $k_r$-axis (outside the strip of absolute convergence). Cauchy's theorem was then applied to this path, resulting in an expression with the correct growth rate. However, the spatially growing $h_B$ (of (2.9)) described in Huerre (2000) is unbounded at $x = \pm\infty$. Having obtained the correct spatial growth rate, Huerre did not continue the analysis to determine whether the remaining portion of the solution ($h_A$ in (2.9)) cancels this unbounded growth. In § 2.2, we show that $h_A$ only cancels pieces of the correctly evaluated $h_B$ that spatially decay towards $x = \pm\infty$. Using a path that lies outside the strip of absolute convergence in the complex $k$-plane, Huerre (somewhat fortuitously) obtained the correct spatial growth rate from the wrong integral. Any path deformation away from the original Fourier inversion path of $h_B$ (in our case, the $k_r$-axis) must be closed back to the original inversion path, and this will inevitably lead to a spatially decaying result for $h_B$ (equation (2.12)). When Gordillo & Pérez-Saborid (2002) compared their (correct) evaluation of $h_B$ with that of Huerre (2000), they incorrectly concluded that the solutions are equivalent.

Although the problem is left non-specific in Bers (1983) and Huerre (1987), the procedures given lead to conclusions that attribute spatial growth to the integral $h_B$. In Huerre & Monkewitz (1990) and Huerre (2000) these procedures were applied to the oscillatory-forced linear Ginzburg–Landau equation. We note that $h_B$, given here by (2.12), is identical in form for both the forced Klein–Gordon equation and the forced Ginzburg–Landau equation; they both spatially damp. A perhaps less demanding (but not general) argument that substantiates the spatial decay of $h_B$, is the absolute integrability (with respect to $k$) of $1/D(k, \omega_f)$ for both the Klein–Gordon and Ginzburg–Landau equations. This ensures, through the Riemann–Lebesgue lemma (Lighthill 1962; Weinberger 1965), that the integral $h_B$ given in (2.9) spatially decays. In the current work, we demonstrate that it is, in fact, the integrals corresponding to $h_A$ in (2.11) that are responsible for spatial growth due to forcing, as correctly identified by Gordillo & Pérez-Saborid (2002).

We now focus on the evaluation of the integrals in (2.11). It is impractical to evaluate $h_A$ using contour integration on the same complex semicircular paths used to evaluate $h_B$. The sign of $[kx - \omega(k)t]$ cannot be readily determined, and so one cannot close the contour in any simple way. Instead, we look for an integration path that enables asymptotic analysis as $t \to \infty$. It is natural, then, to utilize the method of steepest descent. In this method, a path is chosen that passes through saddle points of the argument of the exponential in such a way that the real part of $[k(x/t) - \omega(k)]t$ is constant. This enables the dominant exponential behaviour to be identified along the path as $t$ becomes large, using Laplace's method or Watson's lemma (Bender & Orszag 1978). The complex $k$-plane may contain an infinite number of saddle points, $k_s$, which satisfy $(\partial\omega^{\pm}/\partial k)|_{k_s} = x/t$, each for some real-valued ray $x/t$. In the context of a linear wave problem, each $k_s$–$x/t$ pair can be thought of in the following way: an observer travelling at a velocity $x/t$ will see waves governed by $D[k_s, \omega(k_s)] = 0$, each moving with a phase of $[k_s x - \omega(k_s)t]$ (Whitham 1974). For the Klein–Gordon equation, a fixed $x/t$ ray provides two saddle points, $k_{s\pm}$, which satisfy $\mathrm{Re}((\partial\omega^{\pm}/\partial k)|_{k_s}) = x/t$ and $\mathrm{Im}(\partial\omega^{\pm}/\partial k|_{k_s}) = 0$, where $\partial\omega^{\pm}/\partial k$ is determined

https://doi.org/10.1017/jfm.2012.86 Published online by Cambridge University Press

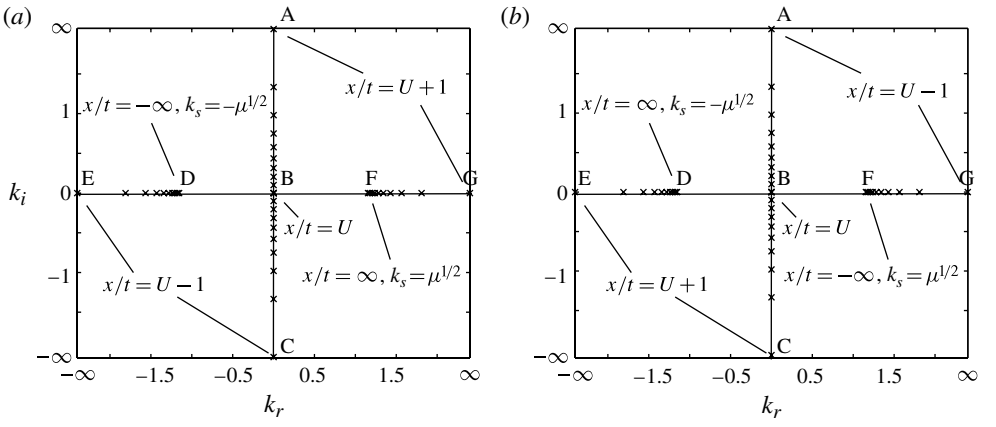



FIGURE 6. Location of saddles (×) for (*a*) $h_A^+$ and (*b*) $h_A^-$, given by (2.13). Here $\mu = 1$, $U = 2$. The saddles are densely populated within each line segment, shown separated here for equal $\Delta(x/t)$. (*a*) AB, $U < x/t < U + 1$; BC, $U - 1 < x/t < U$; ED, $-\infty < x/t < U - 1$; FG, $U+1 < x/t < \infty$. (*b*) AB, $U-1 < x/t < U$; BC, $U < x/t < U+1$; ED, $U+1 < x/t < \infty$; FG, $-\infty < x/t < U - 1$. There are no saddles between D and B or between B and F.

from (2.6). For $U > 1$ and $\mu > 0$, they are given by

$$k_{s\pm} = \pm\frac{\sqrt{\mu}(x/t - U)}{\sqrt{(x/t - U)^2 - 1}}. \tag{2.13}$$

For unstable waves ($\mu > 0$), the numerator of (2.13) is always real. The denominator is either purely real ($|x/t-U| > 1$) or purely imaginary ($|x/t-U| < 1$). This indicates that all saddles either lie on the real axis or the imaginary axis in the $k_i$–$k_r$ plane, leading to sets of saddles, shown in figure 6(*a*) for $h_A^+$ and figure 6(*b*) for $h_A^-$. The saddles along ED, AC and FG, are densely populated. The separation distances between any two saddles in figure 6 are shown for equal $\Delta(x/t)$; this is done only to illustrate the variation of $x/t$, governed by (2.13). As mentioned previously, the saddles $k_s = \pm\sqrt{\mu}$ at D and F are also branch points, making DF the appropriate location to make a branch cut to enable further analysis (Morse & Feshbach 1953). The only other saddle to lie along the line DF is $k_s = 0$, which is also the wavenumber responsible for maximum temporal growth, $\omega_i = \sqrt{\mu}$. This saddle is paired with $x/t = U$, which is consistent with the classical analysis in § 2.1. This maximum growth saddle–ray pair belongs to the locus of saddles along the imaginary axis, which is shown in figure 6. These purely imaginary saddles (line ABC) must be responsible for temporal growth, because all of the real saddles (lines ED and FG) lie outside the temporally unstable region of figure 2. If one wished to track the transient (i.e. temporally growing) solution to this problem, one could focus on the ray $x/t = U$, as done in § 2.1. This ray lies in the centre of the transient region illustrated in figure 1. Based on the saddle locations shown in figure 6, we can now identify the limits of the temporally unstable wave packet as $U - 1 \leqslant x/t < U + 1$. For problems where the saddles are not purely real or imaginary, determination of the temporally unstable saddles is not as mathematically straightforward. However, the procedure is identical conceptually, as we shall see for the liquid sheet problem in § 3.2. For fully complex saddles, the temporally unstable saddles that define the transient region are characterized as having a non-zero 'aggregate growth' $\sigma$, which is the real part of $\mathrm{i}[k_s(x/t) - \omega(k_s)]$ (Gaster

https://doi.org/10.1017/jfm.2012.86 Published online by Cambridge University Press

1968; Monkewitz 1990). The value of $\sigma$ can also be interpreted as the temporal growth rate of a wave taken in a frame of reference moving at a velocity given by the corresponding $x/t$ ray. The characterization of $x/t$ rays based on their corresponding $\sigma$ value is outlined in Huerre (2000) for an impulse response, and is put into the context of the signalling problem in § 2.3.

Evaluation of the steepest descent path through the saddle of maximum aggregate growth usually provides the asymptotic description of waves in the unforced problem as $t \to \infty$ (Barlow *et al.* 2010). However, this saddle does not provide any information about the envelope of steady spatial growth induced by forcing; for that, we will need to consider the spectrum of all possibly growing saddles and identify $x/t$ rays that are critical to determining the ultimate evolution of the forced solution.

The contour used to join the steepest descent path to the original path can often be chosen in a number of ways, provided the contribution along this connecting contour is subdominant and the coefficient of the time-varying exponential is analytic (Lighthill 1978). When (2.11) is evaluated via contour integration, the resultant complex integral is not necessarily analytic everywhere, because there are poles at $\omega^{\pm}(k) = \omega_f$, given by $k_{f1,f2}$ in (2.7) and branch points at $k = \pm\sqrt{\mu}$. If a pole is enclosed between a steepest descent path and the original integration path (the $k_r$-axis) of the integrals in (2.11), the resultant residue can dominate the asymptotic behaviour of the solution. These poles are shown in figure 7, each for a different positive forcing frequency. The trends of complex $k$ corresponding to increasing $\omega_f$ are also shown in figure 7. As $\omega_f$ is increased, the poles become purely real and spatial growth ceases. This occurs when $\omega_f = [\mu(U^2 - 1)]^{1/2}$, shown as point $B$ in figure 7. As $\omega_f$ is increased further, $k_{f2}$ increases along the $k_r$-axis, while $k_{f1}$ decreases along the $k_r$-axis until reaching the branch point ($k_{f1} = \sqrt{\mu}$, $\omega_f = \sqrt{\mu}U$), shown as point $C$ in figure 7. As $\omega_f$ is increased even further, both $k_{f1}$ and $k_{f2}$ increase along the $k_r$-axis.

The existence of these poles requires us to completely determine each path of steepest decent, as it is only then that the relative contributions of the poles and saddle points can be correctly assessed as $t$ becomes large. This is in contrast with the unforced problem, where a single saddle point contribution governs the asymptotic behaviour, and the long time asymptotic behaviour can be deduced solely via a portion of the path in the immediate vicinity of the saddle.

The steepest paths through the saddle points are given by the equation

$$\mathrm{Re}\left[k\frac{x}{t} - \omega^{\pm}(k)\right] = \mathrm{Re}\left[k_s\frac{x}{t} - \omega^{\pm}(k_s)\right] \tag{2.14}$$

where Re denotes the real part of the bracketed argument. For the saddles along the line ABC in figure 6, $\mathrm{Re}[k_s(x/t) - \omega^{\pm}(k_s)] = 0$. Substituting this and (2.6) into (2.14) leads to a family of curves describing the steepest paths, given by

$$k_r\left[\left(\frac{k_r}{a}\right)^2 + \left(\frac{k_i}{\mathrm{Im}(k_s)}\right)^2 - 1\right] = 0 \tag{2.15a}$$

where

$$a = \sqrt{\mu/[(1 + x/t - U)(1 - x/t + U)]} \tag{2.15b}$$

and $k_s$ is given by the purely imaginary saddles (line ABC) shown in figure 6 and determined by (2.13). The above equation describes two paths: $k_r = 0$ (the $k_i$-axis) and an ellipse, shown in figure 8 for saddles lying along lines AB ($SD_{AB}$) and BC ($SD_{BC}$). The path of steepest *descent* passes perpendicular to isocontours of

https://doi.org/10.1017/jfm.2012.86 Published online by Cambridge University Press

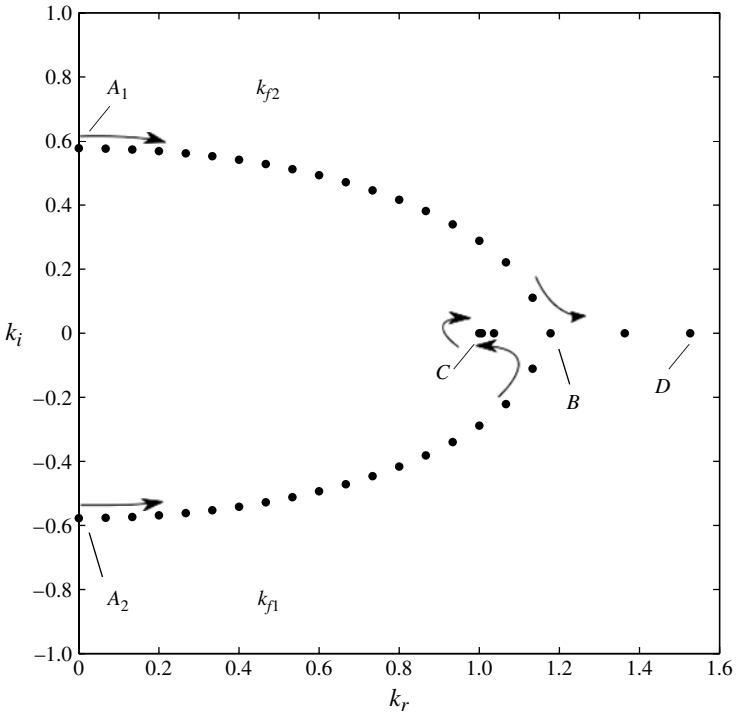



FIGURE 7. Location of poles for $h_A^+$ ($k_{f1}$) and $h_A^-$ ($k_{f2}$), given by (2.7). The real positive forcing frequency increases from $\omega_f = 0$ (points $A_1$ and $A_2$) in the direction of the arrows. When the frequency is increased beyond $\omega_f = [\mu(U^2-1)]^{1/2}$ (point $B$), the spatial poles are purely real; no spatial growth occurs above this frequency. As $\omega_f$ is increased further, $k_{f2}$ increases along the $k_r$-axis towards point $D$, while $k_{f1}$ decreases along the $k_r$-axis until $\omega_f = \sqrt{\mu}U$ and $k_{f1} = \sqrt{\mu}$ (point $C$, branch point). As $\omega_f$ is increased even further, $k_{f1}$ increases along the $k_r$-axis towards point $D$. In this figure, $\mu = 1$ and $U = 2$.

$\mathrm{Im}[k(x/t) - \omega(k)]$ (not shown) that decrease away from the saddle, decreasing the magnitude of the exponential argument in $h_A$ for a given time. For a large time, the main contribution then comes from the saddle point, which is a maximum along this path, and allows for the asymptotic behaviour to be deduced. The other steepest path (that of 'ascent') is not useful for the asymptotic analysis, since the magnitude of the exponential argument increases away from the saddle and leads to a non-converging integral (Morse & Feshbach 1953). For saddles lying along the line ABC in figure 6 for both $h_A^+$ and $h_A^-$, the steepest descent path is the ellipse and the steepest ascent path is the $k_i$ axis; a proof is given in appendix A. For this problem, the steepest descent paths intersect the original path of integration (the real axis) at $k_r = \pm a$ (2.15*b*), eliminating the need for a 'connecting contour' to close the path. If this were not the case, one would need to justify that a subdominant connecting contour exists; examples are given in Bleistein (1984) using Jordan's lemma. We partition the Fourier integral $h_A^\pm = h_{A1}^\pm + h_{A2}^\pm + h_{A3}^\pm$ such that the integration path of each term is, respectively, $\int_{-\infty}^{-a}$, $\int_{-a}^{a}$ and $\int_{a}^{\infty}$, shown in figure 8. The inner piece, $h_{A2}^\pm$, is evaluated by forming a closed path with both the top and bottom semi-ellipses of steepest descent, also shown in the figure. The choice of ellipse is determined by the $x/t$ ray of interest, and its association with either the saddles lying along the lines AB or BC of figure 6. The

https://doi.org/10.1017/jfm.2012.86 Published online by Cambridge University Press

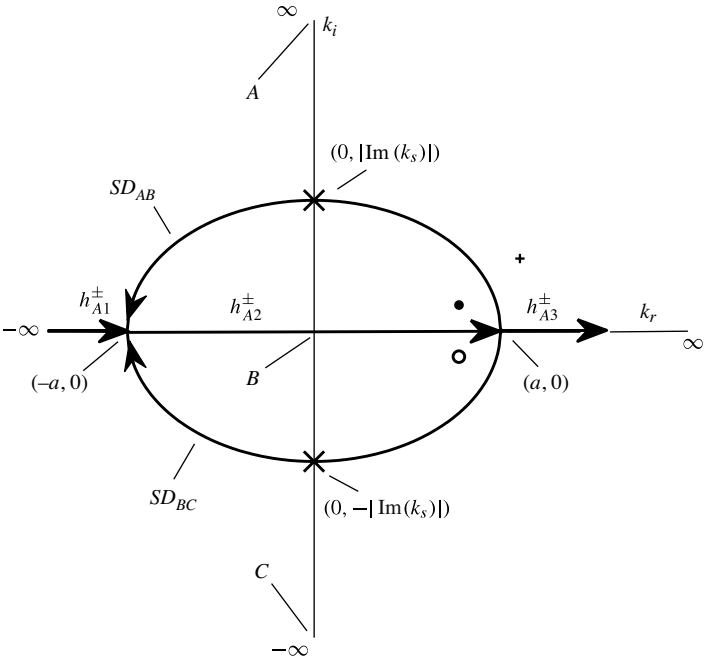



FIGURE 8. Paths of steepest descent (ellipse) and ascent (vertical axis) through saddles (×) lying along the lines AB ($SD_{AB}$) and BC ($SD_{BC}$) for a particular $x/t$ ray. The ellipse intercepts $\pm a$ and $\pm|\mathrm{Im}(k_s)|$ are given by (2.15*b*) and (2.13), respectively. The markers •, + and ∘ indicate possible pole locations (2.7) in relation to the integration path described by (2.17).

closed path formed by $h^{\pm}_{A2}$ and either the upper or lower semi-ellipse equates $h^{\pm}_{A2}$ to the sum of the steepest descent path (taken in the opposite direction) and any pole contributions that are enclosed by the semi-ellipse. For a given $x/t$ ray, the solution then becomes

$$h^{\pm}_A|_{x/t} = h^{\pm}_{A1} - \int_{SD_\pm} + 2\pi\mathrm{i} \sum \text{ residues} + h^{\pm}_{A3} \tag{2.16}$$

where $\int_{SD}$ is the steepest descent path through a saddle associated with a particular $x/t$. By fixing $x/t$ within the range of the saddles lying along the lines AB and BC in figure 6, integration by parts can be directly applied to $h^{\pm}_{A1}$ and $h^{\pm}_{A3}$ to show that they decay like $1/t$ as $t \to \infty$ (Bender & Orszag 1978). The solution is then dominated by the saddle point and pole contributions, leading to the asymptotic result

$$h^{\pm}_A|_{x/t} \sim - \int_{SD_\pm} + 2\pi\mathrm{i} \sum \text{ residues}, \quad t \to \infty. \tag{2.17}$$

The individual residues are multiplied by 1, −1 or 0, depending on whether a $k_f$ pole is enclosed by the ellipse in the upper half-plane (•), enclosed in the lower half-plane (∘) or not enclosed at all (+), as indicated in figure 8. The integration paths for $h_A$ are shown in figure 9(*a–d*) for $h^{+}_A|_{U-1\leqslant x/t<U}$, $h^{-}_A|_{U-1\leqslant x/t<U}$, $h^{+}_A|_{U<x/t\leqslant U+1}$ and $h^{-}_A|_{U<x/t\leqslant U+1}$, respectively. For all plots, a single unstable forcing frequency is chosen and an $x/t$ value is assumed such that the ellipse of steepest descent is large enough to enclose the $k_f$ poles, if they exist in the relevant quadrant. If a stable forcing frequency

https://doi.org/10.1017/jfm.2012.86 Published online by Cambridge University Press

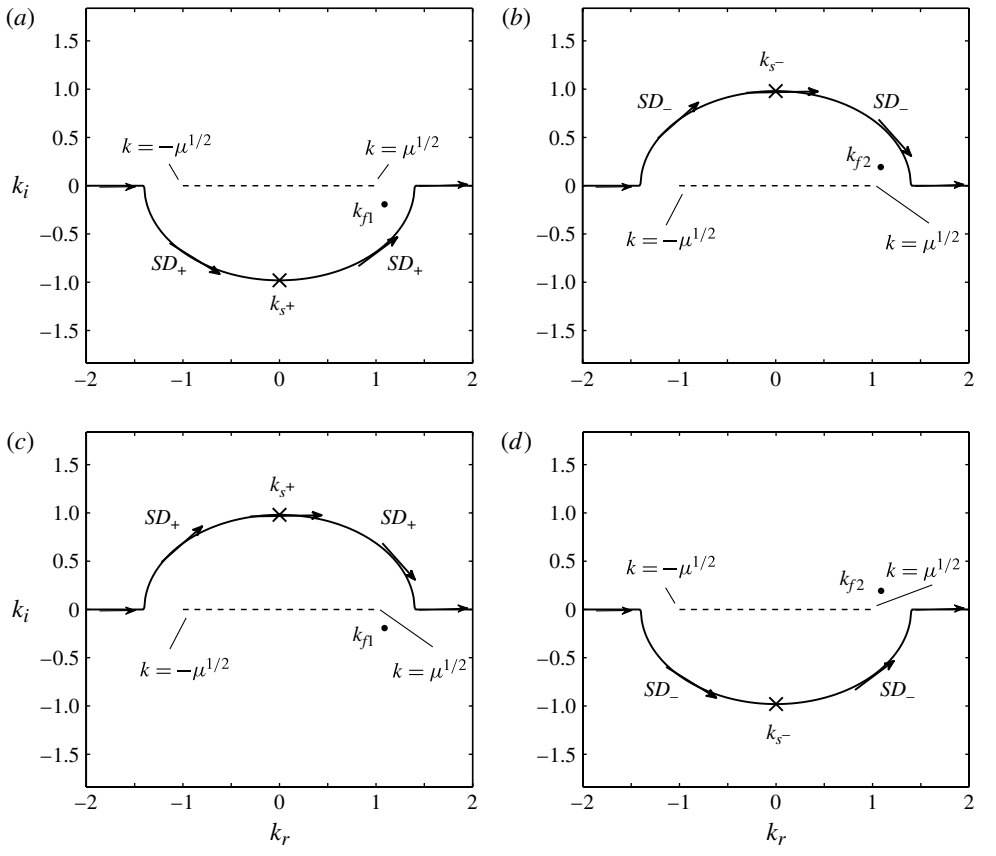



FIGURE 9. Integration paths for $U-1 < x/t < U$, (*a*) $h_A^+$ and (*b*) $h_A^-$, and $U < x/t < U+1$, (*c*) $h_A^+$ and (*d*) $h_A^-$: (×) saddles; (•) poles; (– –) branch cut; $\mu = 1,\ U = 2,\ \omega_f = 1.632$.

is chosen (one that leads to real-valued $k_f$ poles), the residue contribution is replaced by a principal value with half the magnitude. Recall, that it is also possible that a pole is not enclosed by the ellipse, for certain $x/t$ rays (not shown); this 'limiting' process of enclosing poles is important to our problem and is discussed later. The branch cut from $k_r = -\sqrt{\mu}$ to $k_r = \sqrt{\mu}$ is drawn in figure 9 as a dashed line. From (2.15), it is seen that the ellipse of steepest descent intersects the branch cut only for the ray $x/t = U$, that of the fastest growing mode. The classical analysis (§ 2.1) sufficiently describes the behaviour of this ray. Therefore, to avoid passing through the branch cut, we are careful not to directly include the ray $x/t = U$ in our analysis. On the other hand, we do include the rays $x/t = U-1$ and $x/t = U+1$ in the scope of figure 9. Equation (2.15) shows that these particular rays lead to circular paths of steepest descent that pass through two saddles for each part of the solution ($h_A^+$ and $h_A^-$): one saddle at $k_s = \pm\mathrm{i}\infty$ and another at $k_s = \pm\infty$. This effectively bridges the saddles lying along the lines AB and BC, respectively, with the saddles lying along the lines FG and ED in figure 6. It should be noted that (2.17) is exact for $x/t = U-1$ and $x/t = U+1$ for all $t$, since the entire $k_r$-axis closes the circular path. This is discussed further in appendix B, where the contributions of the saddles lying along the lines ED and FG in figure 6 are examined.

https://doi.org/10.1017/jfm.2012.86 Published online by Cambridge University Press

Finally, we can evaluate (2.16) and write the integral solution for $h_A$ in the range $U-1 \leqslant x/t < U$ as

$$[h_A(x,t)]_{\substack{U-1\leqslant x/t<U \\ t\to\infty}} \sim -\left[\int_{SD+}\right]_{x/t} - \left[\int_{SD-}\right]_{x/t} - \mathrm{i}A\frac{\mathrm{e}^{\mathrm{i}(k_{f1}(x/t)-\omega_f)t}}{\left[\dfrac{\partial D}{\partial\omega}\dfrac{\partial\omega}{\partial k}\right]_{k_{f1},\omega_f}} + \mathrm{i}A\frac{\mathrm{e}^{\mathrm{i}(k_{f2}(x/t)-\omega_f)t}}{\left[\dfrac{\partial D}{\partial\omega}\dfrac{\partial\omega}{\partial k}\right]_{k_{f2},\omega_f}} \tag{2.18}$$

where the third term is zero if $k_{f1}$ is not enclosed by $\int_{SD}$ and $\int_{-\infty}^{\infty}$ and the fourth term is zero if $k_{f2}$ is not enclosed. The integral solution for $h_A$ in the range $U < x/t \leqslant U+1$ is

$$[h_A(x,t)]_{\substack{U<x/t\leqslant U+1 \\ t\to\infty}} \sim -\left[\int_{SD+}\right]_{x/t} - \left[\int_{SD-}\right]_{x/t} \tag{2.19}$$

since no poles are enclosed by the paths in figure 9(*c*,*d*). In (2.18) and (2.19), $[\int_{SD\pm}]_{x/t} \sim t^{-1/2}\mathrm{e}^{\mathrm{i}[k_s\pm x/t-\omega^{\pm}(k_s)]t}$ for simple saddles ($\partial^2\omega/\partial k^2|_{k_s} \neq 0$) (Bender & Orszag 1978). Note that the residues in (2.18) have no restriction on the sign of $\mathrm{Im}(k_f)$, in contrast with those of (2.12) where the Heaviside function, used to guarantee convergence, suppresses any spatial growth for $h_B$. The integral responsible for spatial growth is, in fact, $h_A$. From the form of (2.18) and noting that $x/t > 0$, we can now state the necessary and sufficient conditions for downstream spatial growth: (i) $\mathrm{Im}(k_f) < 0$ (signalled by $\omega_f$); (ii) $k_f$ is enclosed by the $k_r$ axis and a steepest descent path through a saddle of the dispersion relation. As indicated by figure 9, poles are enclosed for $U-1 \leqslant x/t < U$, but not for $U < x/t \leqslant U+1$, indicating spatial growth (and decay) to the left of the peak ($x/t = U$) of the transient waveform, but not necessarily to the right. As it happens, the solution is identically zero to the right of the leading edge ($x/t = U+1$) of the transient; this is shown in the following analysis.

We now examine the relationship between saddle and pole location in the complex $k$-plane, in order to understand the extent of the transient region in figure 1, and to develop a closed-form solution in the signalling region. As noted above, a residue is generated in (2.18) when a pole resides between a steepest descent path and the real axis. The integration paths for $h_A^+$ (——) and $h_A^-$ (– –) for the rays $U-1 \leqslant x/t < U$ are shown in figure 10. As $x/t$ decreases, the enclosure of poles (•, ○) occurs for some 'limiting ray', $(x/t)_T$, and for all rays $U-1 < x/t < (x/t)_T$. It should be clarified that this is not the limiting ray at which the transition between steady-state spatial growth and unsteady temporal growth occurs, since contributions from temporally unstable saddle points and spatially growing residues both exist for $U-1 < x/t < (x/t)_T$. We refer to $(x/t)_T$ as the 'transient limiting ray', since all rays $(x/t)_T < x/t < U$ are limited to temporally growing saddle point contributions (no residues are accrued through $h_A$). In the method introduced by Gordillo & Pérez-Saborid (2002), this type of limiting ray is evaluated for simple saddles by first locating the path of steepest descent that passes through both $k_s$ and $k_f$, and then finding the $x/t$ value associated with this path. Applying this procedure to (2.14), one obtains

$$\mathrm{Re}(k_f)\,(x/t)_T - \omega_f = \mathrm{Re}(k_s)\,(x/t)_T - \mathrm{Re}[\omega^{\pm}(k_s)], \tag{2.20}$$

which is exactly the first part of (13) in Gordillo & Pérez-Saborid (2002). Further details concerning $(x/t)_T$ (denoted by $(x/t)_{lim}$ in Gordillo & Pérez-Saborid (2002)) are given in this reference. Substituting (2.13) into (2.20) for the $U-1 \leqslant x/t < U$ set of

https://doi.org/10.1017/jfm.2012.86 Published online by Cambridge University Press

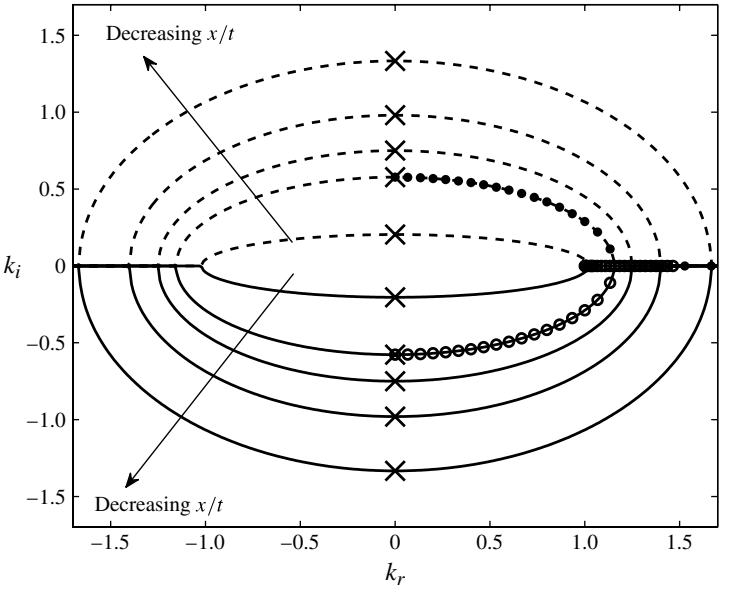



FIGURE 10. Paths of steepest descent through the saddles (×) of $h_A^+$ (——) and $h_A^-$(– –) for $U-1 < x/t < U$. From innermost to outermost ellipse: $x/t = 1.8,\ 1.5,\ 1.4,\ 1.3$ and 1.2. Here $k_{f1}$ (○) and $k_{f2}$ (●) poles, given by (2.7), are shown for range of forcing frequencies, $\omega_f > 0$; $U = 2,\ \mu = 1$.

saddles leads to

$$(x/t)_T = U - \frac{1}{U} \tag{2.21}$$

which is independent of the forcing frequency $\omega_f$. The ellipse associated with this ray is easily determined by substituting (2.21) into (2.15). As shown in figure 10, the limiting ellipse for $h_A^+$ falls along the path of all poles that lead to spatial growth ($k_{f1}$, denoted by ○ in the figure). For $U-1 \leqslant x/t < (x/t)_T$ there is competition between the transient saddle point contribution and the steady spatial-growth pole contribution. The transient contribution becomes smaller as $x/t$ decreases from $U$ to $U-1$. For $x/t$ slightly above $U-1$, $k_s$ is still within the temporally unstable regime of saddles (i.e. along line BC in figure 6*a* and along line AB in figure 6*b*). For $x/t$ slightly below $U-1$, $k_s$ lies in the temporally stable regime of saddles (i.e. along line ED in figure 6*a*, and along line FG in figure 6*b*). This suggests that the 'spatial-growth limiting ray' is given by $(x/t)_S = U-1$.

Even though there is no temporal growth associated with the real-valued saddles, in appendix B we show that spatial growth is present for $0 < x/t < U-1$, when forced at particular forcing frequencies. By applying Cauchy's integral theorem and using our knowledge of the placement of real-valued saddles, we show that $h_A^-$=0 and $h_A^+$ is given by (B 4) for $x/t \to (U-1)^-$. The solution, $h = h_A^+ + h_B$, for the spatially growing forced region is then given by the superposition of (B 4) and (2.12):

$$[h(x,t)]_{x/t\to(U-1)^-} = -\mathrm{i}A\frac{\mathrm{e}^{\mathrm{i}(k_{f1}(x/t)-\omega_f)t}}{\left[\dfrac{\partial D}{\partial\omega}\dfrac{\partial\omega}{\partial k}\right]_{k_{f1},\omega_f}} + \mathrm{i}A\frac{\mathrm{e}^{\mathrm{i}(k_{f2}(x/t)-\omega_f)t}}{\left.\dfrac{\partial D}{\partial k}\right|_{k_{f2},\omega_f}}. \tag{2.22}$$

https://doi.org/10.1017/jfm.2012.86 Published online by Cambridge University Press

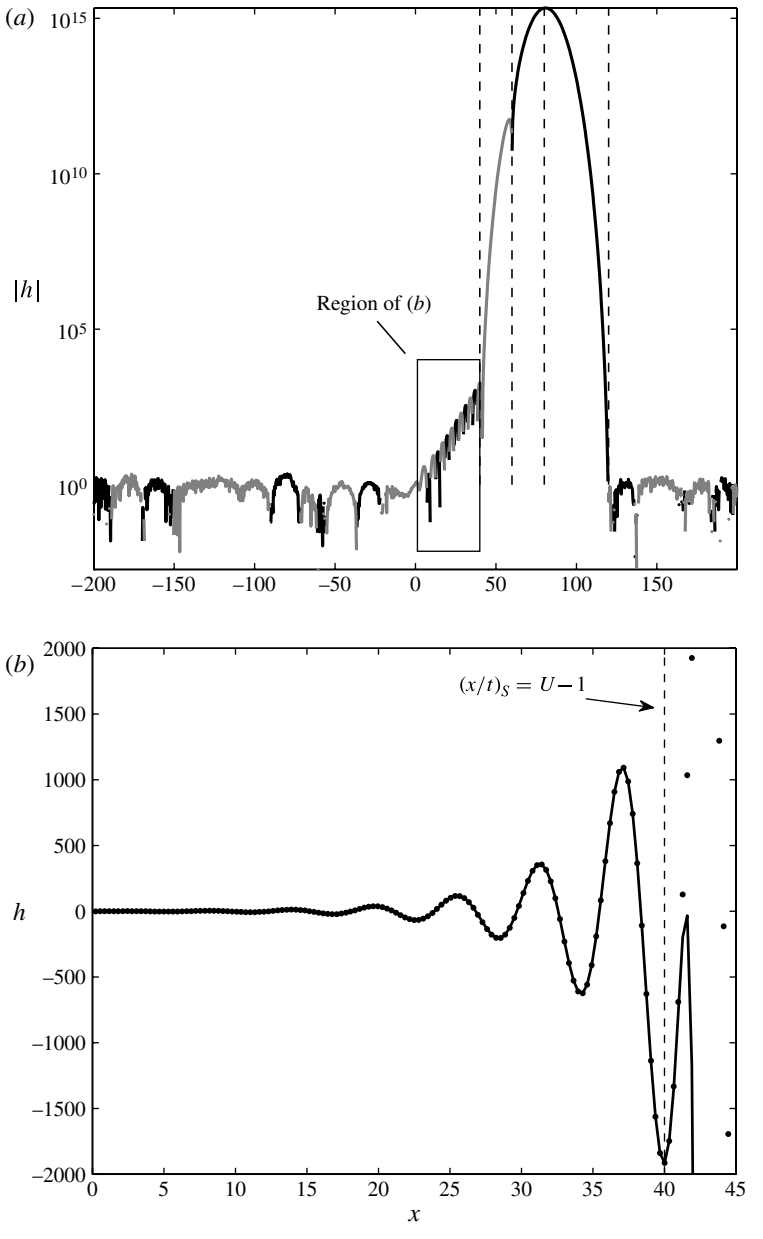



FIGURE 11. Series solution of (2.1) at $t = 40$ with $\mu = 1$, $U = 2$ and $\omega_f = 1.632$. (*a*) Rays (– –) from left to right: $(x/t)_S = U - 1$, $(x/t)_T = 1.5$, $x/t = U$ and $(x/t)_F = U + 1$. (*b*) Magnification showing the steady-state spatially growing region. The series solution (——) exactly matches the residue prediction (•) given by (2.22).

Although (2.22) is given in the limit as smaller $x/t$ values approach $x/t = U - 1$, we expect that it is valid for the entire range $0 < x/t < U - 1$. The series solution verifies the result (2.22), shown in figure 11. In figure 11(*a*), the wave height is provided on a logarithmic scale and negative values are shaded in grey. Apart from the logarithmic scale, figures 11 and 4(*a*) are identical. The ray of maximum growth ($x/t = U$) and the

https://doi.org/10.1017/jfm.2012.86 Published online by Cambridge University Press

limiting rays which separate important regions of the domain are shown as vertical dashed lines. Figure 11(*b*) shows that the residue prediction (•) of (2.22) is an exact match with the series solution (——) in the steady spatially growing region. This provides us with (at least) two physical interpretations: (i) for a fixed time, the oscillatory-forced spatially growing region is entered as one moves closer to the source ($x = 0$); (ii) for a fixed location, the oscillatory-forced spatially growing region eventually arrives and remains for all time. These interpretations are entirely consistent with figure 1, and are expected, considering the nature of convectively unstable flows, which indicate that transients eventually leave any finite region. While this insight is significant by itself, it is useful to know the exact location (interpretation i) or time (interpretation ii) at which the spatially growing region is observed, which also indicates when the 'unsteady' transient has left the $(x, t)$ coordinate of interest.

For the range of saddles that never enclose a pole ($U < x/t \leqslant U + 1$), it can be seen that $x/t = U + 1$ is also a limiting ray, $(x/t)_F$, that tracks the 'front' of the transient. An expression for $h_A$ beyond this region is obtained by applying Cauchy's integral theorem and again using our knowledge of the placement of real-valued saddles. This is done in appendix B, where we show that $h_A^+ = 0$ and $h_A^-$ is given by (B 9) for $x/t \to (U+1)^+$. The solution, $h = h_A^- + h_B$, for waves beyond the transient is then given by the superposition of (B 9) and (2.12):

$$[h(x,t)]_{x/t\to(U+1)^+} = \mathrm{i}A\frac{\mathrm{e}^{\mathrm{i}(k_{f2}(x/t)-\omega_f)t}}{\left[\dfrac{\partial D}{\partial\omega}\dfrac{\partial\omega}{\partial k}\right]_{k_{f2},\omega_f}} + \mathrm{i}A\frac{\mathrm{e}^{\mathrm{i}(k_{f2}(x/t)-\omega_f)t}}{\left.\dfrac{\partial D}{\partial k}\right|_{k_{f2},\omega_f}} = 0. \tag{2.23}$$

Although (2.23) is given in the limit as larger $x/t$ values approach $x/t = U + 1$, we expect that it is valid for the entire range $U + 1 < x/t$. The two terms in (2.23) are equal and opposite, since $[(\partial D/\partial\omega)(\partial\omega/\partial k)]_{k_{f2},\omega_f} = -\partial D/\partial k|_{k_{f2},\omega_f}$. Thus, the sum is equal to zero, indicating that beyond $(x/t)_F$, the medium is calm.

For the linear forced Klein–Gordon equation, the limiting rays $(x/t)_S$ and $(x/t)_F$ that enclose the transient are exactly the characteristic velocities of (2.1), which is expected because the operator is second-order hyperbolic. Dispersive non-hyperbolic wave problems, in which characteristic velocities do not exist, are examined in § 3.

### 2.3. *Ray extraction method*

In the previous section, the key saddles, integration paths and limiting rays are explicitly obtained for the forced linear Klein–Gordon equation (2.1). For most wave problems, this is an arduous task and often unnecessary for examining the full behaviour, since series solutions are fairly straightforward to generate for many linear wave systems (Barlow *et al.* 2010; Barlow, Helenbrook & Lin 2011). Although one may certainly estimate the region of spatial growth using numerical or series solutions, the limiting rays provide an exact prediction of the location of this region at any given time. In this section, we provide a method that allows one to extract the limiting rays of the signalling problem using only the dispersion relation.

Before giving the full details of the technique, let us first summarize some crucial concepts. Limiting rays are paired with limiting saddles through the growth/phase argument $\mathrm{i}[k_s(x/t) - \omega(k_s)]$, which is used to evaluate the asymptotic behaviour. To extract these rays, a map of saddles can be constructed in the complex $k$-plane, defined by $\mathrm{Im}(\partial\omega/\partial k|_{k_s}) = 0$. Once the relevant sets of saddles $k_s$ are available, the corresponding rays are simply given by $x/t = \mathrm{Re}(\partial\omega/\partial k|_{k_s})$. As mentioned in § 2.2, the aggregate growth of the solution along each ray is determined

https://doi.org/10.1017/jfm.2012.86 Published online by Cambridge University Press

by $\sigma = \mathrm{Re}\{\mathrm{i}[k_s(x/t) - \omega(k_s)]\}$. The rays $(x/t)_S$ and $(x/t)_F$ are defined as follows:

$$\sigma \neq 0 \quad \text{if } |x/t| > (x/t)_S \tag{2.24a}$$

$$\sigma = 0 \quad \text{if } |x/t| < (x/t)_S \tag{2.24b}$$

$$\sigma = 0 \quad \text{if } |x/t| > (x/t)_F \tag{2.25a}$$

$$\sigma \neq 0 \quad \text{if } |x/t| < (x/t)_F\,. \tag{2.25b}$$

The above definitions also apply to the response of a non-oscillatory impulsively forced medium (i.e. the Green's function) (Gaster 1968; Monkewitz 1990; Huerre 2000). For example, when the forcing is given by $A\delta(x)\delta(t)$, the rays $(x/t)_S$ and $(x/t)_F$ represent the trailing and leading edges of the full response. In the cases studied herein, where the forcing is given by $A\delta(x)\mathrm{e}^{-\mathrm{i}\omega_f t}$, the rays $(x/t)_S$ and $(x/t)_F$ represent the trailing and leading edges of the transient region (cf. figure 1). In addition, the ray $(x/t)_T$ predicts where the saddle and pole contributions cease to compete. For $x/t > (x/t)_T$, the solution is dominated by the transient response (cf. figure 1). The saddle $k_s$ associated with $(x/t)_T$ has a steepest descent path that passes through the pole $k_f$ associated with a given $\omega_f$. This is the ray moving slowest away from the source, for which the steepest descent path does not enclose a $k_f$ pole. As proposed by Gordillo & Pérez-Saborid (2002), $(x/t)_T$ is calculated by equating the steepest descent curve through $k_s$ with the steepest decent curve through $k_f$; this is given by (2.20).

In the following procedure, we combine definition (2.24) and (2.25) with the ray extraction technique of Gordillo & Pérez-Saborid (2002), so that one may predict the full behaviour of an oscillatory-forced convectively unstable flow.

(*a*) *Step* 1. Determine the real wavenumber $k_{max}$ associated with the maximum temporal growth rate using the conditions $\partial\omega_i/\partial k_r|_{k_{max}} = 0$ and $\omega_i > 0$. If the dispersion relation can be solved explicitly for $\omega(k)$, $k_{max}$ is easily obtained from a temporal amplification plot. This is given in figure 2 for the Klein–Gordon equation, where $k_{max} = 0$. Note that $k_{max}$ is, by definition, a saddle point.

(*b*) *Step* 2. Construct a grid of $(k_r, k_i)$ values that include $k_{max}$ as an interior point; it is expected that other saddles will lie nearby. Calculate the $\omega(k)$ roots of $D(k, \omega) = 0$ for each grid point. The goal here is to choose the range of $k_i$ and $k_r$ so that the saddles associated with $(x/t)_S$, $(x/t)_F$ and $(x/t)_T$ are either within the domain or are resolved to a desired accuracy. Since we have not yet determined these rays, this step is iterative.

(*c*) *Step* 3. Calculate $\partial\omega/\partial k$ for each $k$ value, make a contour plot of $\mathrm{Im}(\partial\omega/\partial k|_{k_s})$ on the $k_r$–$k_i$ grid, and identify the zero contours; these are the locus of saddle points. For problems such as the Klein–Gordon equation, where branch points are present, it is useful to write $\partial\omega/\partial k|_{k_s}$ in complex polar form, as done in (A 6) (appendix A). This allows one to draw continuous contours of $\mathrm{Im}(\partial\omega/\partial k|_{k_s})$ separately for each Riemann surface. The contours for one Riemann surface of $\mathrm{Im}(\partial\omega^+/\partial k|_{k_s})$ for the Klein–Gordon equation is shown in figure 12(*a*); the zero contours (locus of saddles) are shown in bold. Although it is not shown here, both Riemann surfaces share the same zero contours of $\mathrm{Im}(\partial\omega^+/\partial k|_{k_s})$. The $x/t$–$k_s$ distribution for the first and second Riemann surfaces are different; however, the limiting rays of each surface are the same. Note that the plot in figure 12(*a*) is identical to figure 6(*b*), which was obtained explicitly through (2.13) for $h_A^-$.

(*d*) *Step* 4. The $\mathrm{Im}(\partial\omega/\partial k) = 0$ curves from step 3 provide one with an array of complex wavenumbers. For a given $k_r$ value, its corresponding $k_i$ value is

https://doi.org/10.1017/jfm.2012.86 Published online by Cambridge University Press

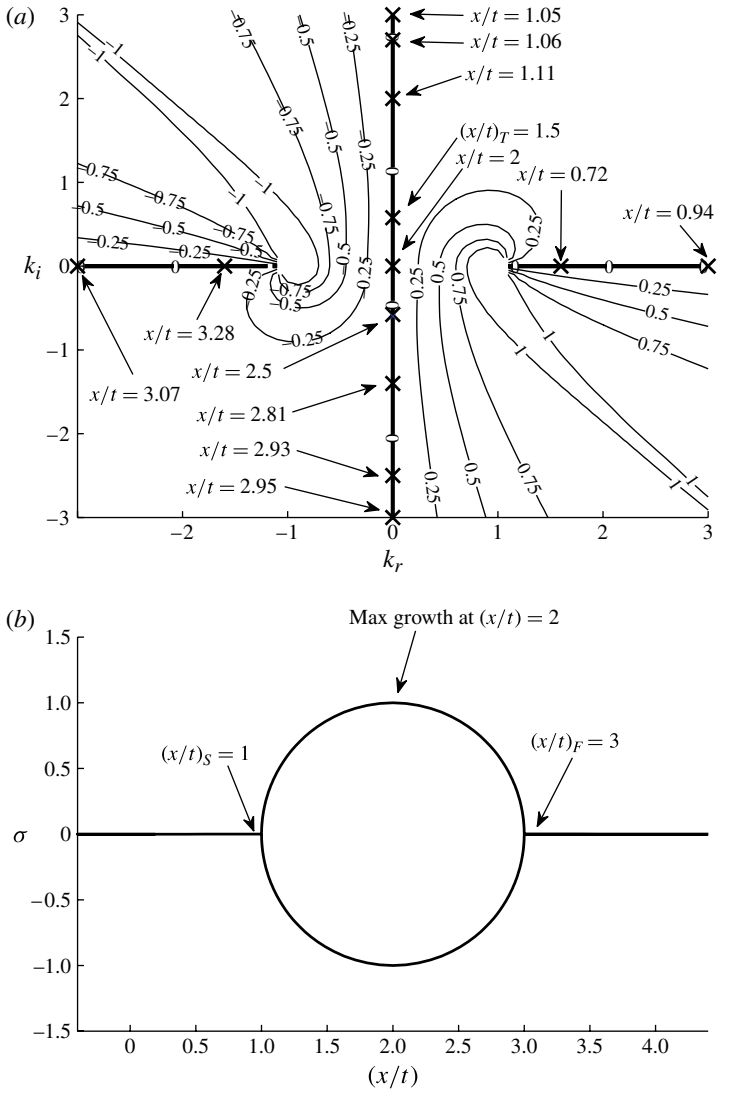



FIGURE 12. The $k_s$–$x/t$ distribution for the forced Klein–Gordon equation with $U = 2$ and $\mu = 1$, determined from $D(k, \omega) = 0$ in (2.4). (*a*) Labelled contours of $\mathrm{Im}(\partial\omega/\partial k)$; zero contours (shown in bold) indicate the locus of saddles. Relevant saddles ($\times$) are labelled with their $x/t$ value. Here $(x/t)_T$ is obtained by solving (2.20). (*b*) Aggregate growth ($\sigma$) versus $x/t$, indicating the values of $(x/t)_S$ and $(x/t)_F$.

established along one of these curves, and the saddle $k_s = k_r + \mathrm{i}k_i$ is identified. This array of saddles can be inserted into the additional definition of a saddle point, $x/t = \mathrm{Re}(\partial\omega/\partial k|_{k_s})$, which provides an array of $x/t$ values. Using both the saddle point and $x/t$ arrays, one can then obtain an array of $\sigma = \mathrm{Re}\{\mathrm{i}[k_s(x/t) - \omega(k_s)]\}$ values for each Riemann surface.

(*e*) *Step* 5. Finally, one can plot $\sigma$ versus $x/t$ and immediately determine the values of $(x/t)_S$ and $(x/t)_F$ by using definition (2.24) and (2.25). This is shown for the Klein–Gordon equation in figure 12(*b*). Here, we are only interested in the

https://doi.org/10.1017/jfm.2012.86 Published online by Cambridge University Press

positive values of $\sigma$; negative values are shown in figure 12(*b*) to remind us that $\sigma$ is multi-valued. The limiting ray values shown in figure 12(*b*) agree with those found in § 2.2. Note that, for this particular problem, the wavenumbers associated with the saddles for $(x/t)_S$ and $(x/t)_F$ do not have finite values (cf. figure 6), and so they can only be approached in a limiting sense. We shall see that this is not the case for the liquid sheet problem in § 3. The ray $(x/t)_T$ is determined by evaluating (2.20), using the saddle point and $x/t$ arrays constructed in step 4, and a $k_f$ value determined from the dispersion relation with a chosen $\omega_f$.

In addition, for a given integral solution

$$h(x,t) = \frac{1}{4\pi^2}\int_{-\infty}^{\infty}\int_{-\infty+i\tau_0}^{\infty+i\tau_0} \frac{f(k,\omega)\mathrm{e}^{\mathrm{i}(kx-\omega t)}}{(\omega-\omega_f)D(k,\omega)}\,\mathrm{d}\omega\,\mathrm{d}k, \tag{2.26}$$

where $f(k,\omega)$ is an arbitrary function that contains no singularities and the path is taken along the real $k$-axis, the steady spatial growth envelope can be approximated by the leading-order contributions of the residue series

$$h\,(x,t)_{|x/t|<(x/t)_S} \sim \sum_{k_f} \mathrm{i}\frac{f(k_f,\omega_f)\mathrm{e}^{\mathrm{i}(k_f(x/t)-\omega_f)t}}{\left.\dfrac{\partial D}{\partial k}\right|_{k_f,\omega_f}}, \tag{2.27}$$

which is a generalization of (2.22), combining the relevant contributions $h_A$ (spatial growth) and $h_B$ (spatial decay). For a particular forcing frequency $\omega_f$, one should first determine the location of the $k_f$ poles in the complex $k$-plane. This indicates the sign of the residue associated with each pole (cf. figure 9). The complete prediction for the region $x/t < (x/t)_S$ for the forced linear Klein–Gordon equation is given by (2.22), and is shown in figure 11(*b*) by •. This approximation provides a simple transfer function between the input forcing and the output waveform. If one is not concerned with the initial transient, the only information needed to describe the asymptotic behaviour of the solution is provided by (2.27), where $x/t < (x/t)_S$ gives the region of validity. Note that this is only ensured for a convectively unstable case, where we are confident that the transient response convects away from the source, leaving only the forced oscillatory response behind.

## 3. Signalling in a liquid sheet

A brief review of the stability of liquid sheets and its applications is given by Lin & Jiang (2003) and Barlow *et al.* (2011). Here we mention only the work that is directly relevant to this study. As shown in the analysis of Rayleigh (1896), there are two linearly independent wave modes of a liquid sheet. The sinuous mode moves the two free surfaces of a sheet in phase. The varicose mode symmetrically moves the free surfaces in opposite directions. These modes were later confirmed in the experiments of Taylor (1959). The onset of wave instability was analysed by Squire (1953) through the use of classical temporal stability theory. The classical theory predicts, for finite $Q = \rho_g/\rho_l$ ($\rho_g$ and $\rho_l$ being, respectively, the gas and liquid densities), that varicose waves are temporally unstable. In addition, sinuous waves are temporally unstable if the Weber number is greater than one. The Weber number is defined as $We = \rho_l U^2 h_0/S$, where $U$ is the liquid velocity in the sheet, $h_0$ is the half-sheet thickness, and $S$ is the interfacial tension. This instability has since been classified as convective; the spatio-temporal analysis can be found in Lin (2003). A sheet subject to an impulsive initial velocity disturbance can also become unstable

https://doi.org/10.1017/jfm.2012.86 Published online by Cambridge University Press

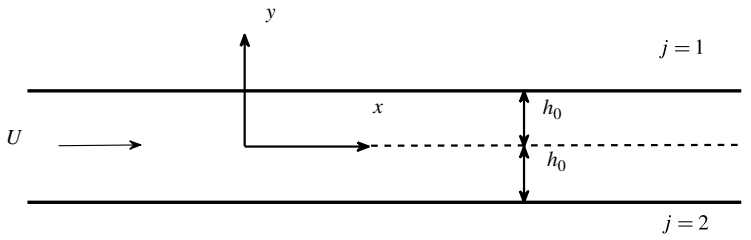



FIGURE 13. Definition sketch, a sheet with uniform thickness.

when $We < 1$, due to an algebraic absolute instability (Barlow *et al.* 2011). However, here we limit our study to $We > 1$, since we are studying prediction mechanisms for forced oscillatory flow, which are only relevant in a convectively unstable medium.

### 3.1. *Formulation*

Consider an inviscid liquid sheet of uniform thickness, $2h_0$, in an inviscid ambient gas of density, $\rho_g$. The gas is stationary and the liquid is flowing at a constant velocity, $U$. The fluids are assumed incompressible and the perturbed flow is assumed to be irrotational, and thus the flow potential, $\phi$, is governed by the Laplace equation, given respectively for the liquid and the gas as

$$(\partial_{xx} + \partial_{yy})\phi_l = 0 \tag{3.1}$$

and

$$(\partial_{xx} + \partial_{yy})\phi_j = 0 \quad (j = 1, 2) \tag{3.2}$$

where $(x, y)$ are the Cartesian coordinates in the unit of half-sheet thickness, $x$ being the flow direction and $y$ perpendicular to the flow. The indices $j = 1$ and 2 refer to the gas above and below the liquid sheet, respectively (cf. figure 13). An oscillating pressure disturbance, $A\delta(x)\mathrm{e}^{-\mathrm{i}\omega_f t}$, is introduced at $x = 0$. To induce sinuous waves at the outset, the pressure disturbance is applied in the same direction to both the top and bottom surfaces of the sheet. To induce varicose waves, the pressure disturbance is applied in opposing directions to the top and bottom surfaces. Typical disturbances may be viewed as a linear combination of these motions. Here, we examine sinuous and varicose modes separately. Through the application of appropriate boundary conditions to the liquid, we allow the sign of $A$ to be arbitrary and derive the dispersion relations for each mode separately. The linearized balance of pressure difference at each interface with the surface tension force provides the dynamic boundary condition,

$$\left[Q\partial_t\phi_j - (\partial_t + \partial_x)\phi_l + A\delta(x)\mathrm{e}^{-\mathrm{i}\omega_f t}\right]_{y=(-1)^{j+1}} = (-1)^j\, We^{-1}\partial_{xx}h_j \quad (j = 1, 2) \tag{3.3}$$

where $h_1$ and $h_2$ are the distances measured in the unit of $h_0$ from the $x$-axis to the upper and lower liquid–gas interfaces, respectively, and time is normalized by $h_0/U$. The linearized kinematic boundary conditions are

$$[\partial_y\phi_l]_{y=(-1)^{j+1}} = (\partial_t + \partial_x)h_j \tag{3.4}$$

$$[\partial_y\phi_j]_{y=(-1)^{j+1}} = \partial_t h_j \quad (j = 1, 2). \tag{3.5}$$

https://doi.org/10.1017/jfm.2012.86 Published online by Cambridge University Press

To ensure that the solution is bounded in the gas above the liquid sheet where $y > 1$ and below the liquid sheet where $y < -1$, a boundedness condition is given by

$$\phi_j(x, y, t) \to 0 \quad \text{as } y \to \left[(-1)^{j+1}\,\infty\right] \quad (j = 1, 2). \tag{3.6}$$

For the sinuous mode of solution, $\phi_l$ is an odd function and the two free surfaces move in unison; this 'odd' boundary condition is given by

$$\partial_{yy}\phi_l(x, y = 0, t) = 0. \tag{3.7}$$

For the varicose mode of solution, $\phi_l$ is an even function and the two free surfaces move in opposite directions; this 'even' boundary condition is given by

$$\partial_{y}\phi_l(x, y = 0, t) = 0. \tag{3.8}$$

3.1.1. *Integral solution*

The double integral solution to this problem is obtained by first Fourier transforming the system (3.2)–(3.5) and applying the boundary conditions (3.6)–(3.8) in Fourier space to solve for the coefficients. The Laplace transform is then applied to the resultant characteristic equation and the doubly transformed interface height is solved for explicitly. Finally, the original variable $h$ is recovered through successive inverse Fourier and Laplace transforms. This process is carried out in Barlow *et al.* (2011) for the unforced sheet. For the forced sheet, the integral solution of the linearized system is given by

$$h(x, t) = \frac{1}{4\pi^2}\int_{-\infty}^{\infty}\int_{-\infty+i\tau_0}^{\infty+i\tau_0}\left[H_0(k, \omega) + \frac{Aik}{(\omega - \omega_f)D(k, \omega)}\right]\mathrm{e}^{\mathrm{i}(kx-\omega t)}\,\mathrm{d}\omega\,\mathrm{d}k \tag{3.9}$$

for $t \geqslant 0$; $h(x, t) = 0$ for $t < 0$. The dispersion relations for the sinuous and varicose modes (Barlow *et al.* 2011) are given respectively by

$$D(k, \omega) = \mathrm{sgn}(k_r)Q\omega^2 + \tanh(k)\,(k - \omega)^2 - We^{-1}k^3 \tag{3.10}$$

and

$$D(k, \omega) = \sinh(k)\mathrm{sgn}(k_r)Q\omega^2 + \cosh(k)\,(k - \omega)^2 - \sinh(k)We^{-1}k^3. \tag{3.11}$$

In (3.9), the unforced contribution $H_0(k, \omega)$ is determined by the initial conditions, and is given by (2.23) in Barlow *et al.* (2011). The second term in (3.9) is the forcing contribution. Since the full solution is the superposition of the forced and unforced solution, there is no need to repeat the analysis of Barlow *et al.* (2011) for the unforced problem. We consider a forced sheet that is initially undisturbed, reducing (3.9) to

$$h(x, t) = \frac{1}{4\pi^2}\int_{-\infty}^{\infty}\int_{-\infty+i\tau_0}^{\infty+i\tau_0}\frac{Aike^{\mathrm{i}(kx-\omega t)}}{(\omega - \omega_f)D(k, \omega)}\,\mathrm{d}\omega\,\mathrm{d}k, \quad t \geqslant 0 \tag{3.12}$$

where the integration path is taken along the real $k$-axis. Note that (3.12) has a form identical to (2.8), excluding the factor of $k$ in the numerator of the integrand.

3.1.2. *Series solution*

In what follows, we examine the behaviour of (3.12) using the ray extraction technique of § 2.3. First, however, we obtain the Fourier series solution of the system (3.2)–(3.8) to assess the efficacy of the technique. As done in § 2.1, the series

https://doi.org/10.1017/jfm.2012.86 Published online by Cambridge University Press

solution is found by solving the system as a boundary value problem, using periodic boundary conditions: $h(-L, t) = h(L, t)$. The Fourier series solution of the linearized system that describes an initially undisturbed forced liquid sheet is given by

$$h(x,t) = \frac{A}{2L} \times \sum_{n\in[-N,-1;1,N]} \frac{\left[\cosh\left(\frac{\Delta_n}{2}t\right) + (b_n - 2\mathrm{i}a_n\omega_f)\sinh\left(\frac{\Delta_n}{2}t\right)/\Delta_n\right]\mathrm{e}^{-t/2a_n} - \mathrm{e}^{-\mathrm{i}\omega_f t}}{D(k_n, \mathrm{i}\omega_f)}\mathrm{e}^{\mathrm{i}k_n x} \tag{3.13}$$

where $k_n = n\pi/L$, $\Delta_n = \sqrt{b_n^2 - 4a_n c_n}$, and

$$a_n = Q/|k_n| + f(k_n)/k_n \tag{3.14a}$$

$$b_n = 2\mathrm{i}\, f(k_n) \tag{3.14b}$$

$$c_n = -k_n\, f(k_n) + k_n^2/We. \tag{3.14c}$$

For sinuous waves, $D(k_n, \mathrm{i}\omega_f)$ is found using (3.10) and $f(k_n) = \tanh(k_n)$. For varicose waves, $D(k_n, \mathrm{i}\omega_f)$ is found using (3.11) and $f(k_n) = \coth(k_n)$. The mode $n = 0$ is excluded from (3.13) because the eigenfunction takes a different form such that $h(x,t)|_{n=0} = 0$.

### 3.2. *Asymptotic predictions and forced solutions*

In this section, the method outlined in § 2.3 is used to predict the key features of convectively unstable waves ($We > 1$, $Q \neq 0$) in a liquid sheet. These features include the limiting $x/t$ rays that bound the transient ($(x/t)_S$ and $(x/t)_F$), the ray that indicates where the transient and forced solution compete for dominance ($(x/t)_T$, which lies in the transient region; cf. figure 1), and the resulting forced response at long time. The predictions are validated by the series solution (3.13).

For small $k$ (long waves) and $Q = 0$, Lin (2003) derived a hyperbolic evolution equation for sinuous waves in a sheet, with characteristic velocities $x/t = 1 \pm We^{-1/2}$. For water sheets surrounded by air (at sea level), $Q = 0.0013$, which is small enough for long waves to be approximated along these characteristic rays. For $We > 1$, the characteristic rays indicate that sinuous waves propagate downstream from an initial disturbance. In § 2.2 we determined that, for the hyperbolic Klein–Gordon equation, the rays which enclose the transient ($(x/t)_S$ and $(x/t)_F$) are exactly equal to the characteristic velocities of (2.1). To illustrate how limiting rays in a non-hyperbolic dispersive system deviate from the characteristic rays of the hyperbolic limiting behaviour (given above), we examine sinuous waves in a sheet for $Q = 0.0013$ and $Q = 0.13$. We also examine the limiting rays for varicose waves with $Q = 0.13$. The results for the varicose case are of particular interest, since there are no characteristic velocities in the long wavelength limit (Lin 2003). In all cases examined here, $We = 20$.

For the three cases to be examined, temporal amplification plots are shown in figure 14; these are obtained through $D(k, \omega) = 0$ in (3.10) and (3.11). The maximum growth saddles are indicated in each plot. Note that all plots in figure 14 are symmetric about the $k_i$-axis. This is a consequence of the $\mathrm{sgn}(k_r)$ function appearing in the dispersion relations, resulting in maximum growth at both $\pm k_r$ values.

Using the location of the maximum growth saddles in figure 14 as a starting point, the temporal growth saddles are found using the method given in § 2.3. These are

https://doi.org/10.1017/jfm.2012.86 Published online by Cambridge University Press

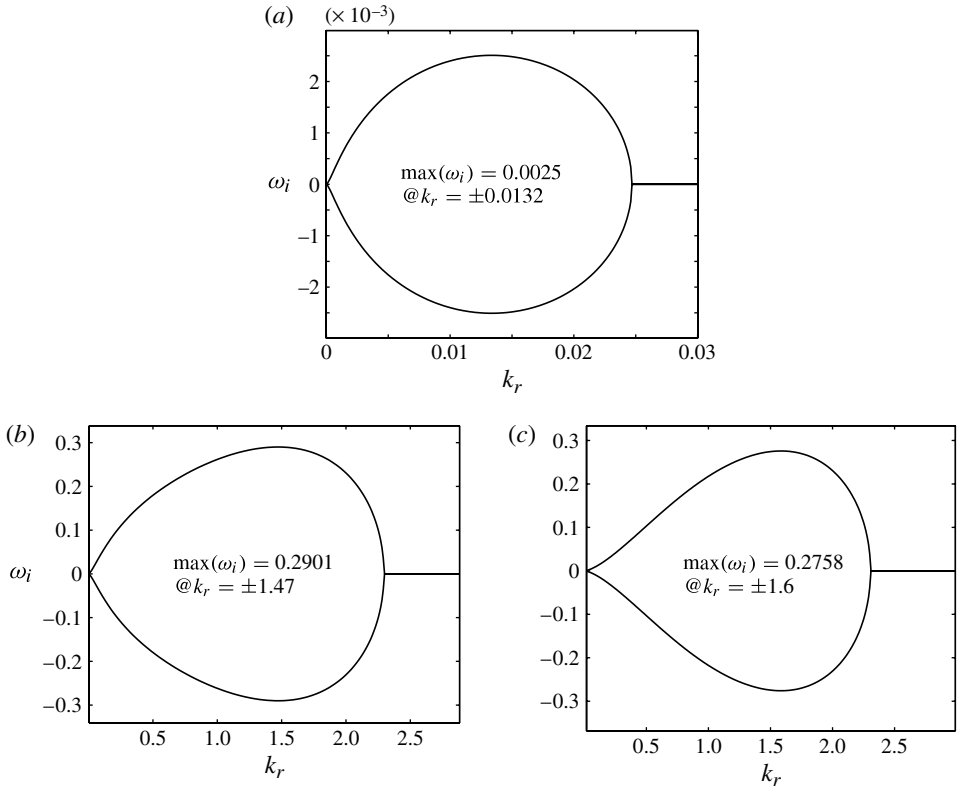



FIGURE 14. Temporal amplification curves for sinuous waves, given by $D(k, \omega) = 0$ in (3.10): (*a*) $Q = 0.0013$, $We = 20$ and (*b*) $Q = 0.13$, $We = 20$. (*c*) Temporal amplification curve for varicose waves, given by $D(k, \omega) = 0$ in (3.11) with $Q = 0.13$, $We = 20$. All plots are symmetric about the $k_i$-axis. For each plot, the maximum growth saddles are indicated, where $\partial\omega_i/\partial k_r = 0$.

shown for sinuous waves ($Q = 0.0013$, $Q = 0.13$) and varicose waves ($Q = 0.13$) in figures 15(*a*), 16(*a*) and 17(*a*), respectively. One striking difference between these saddle maps and that of the Klein–Gordon equation (figure 12), is the 'finite' location where the complex saddles meet the purely real saddles. As one might predict from the analysis of the Klein–Gordon equation, these saddles correspond with the limiting rays $(x/t)_S$ and $(x/t)_F$, which is confirmed in the aggregate growth plots of figures 15(*b*), 16(*b*) and 17(*b*).

The saddle associated with the transient limiting ray $(x/t)_T$ is shown in figures 15(*a*), 16(*a*) and 17(*a*), and is computed by applying (2.20) to $D(k, \omega) = 0$ in (3.10) and (3.11) for sinuous and varicose waves, respectively. The approximated characteristic rays $x/t = 1 \pm We^{-1/2}$ (for sinuous waves) are also shown in figures 15(*a*) and 16(*a*). For $Q = 0.0013$ (figure 15*a*), the characteristic ray $x/t = 1 - We^{-1/2} = 0.7764$ is a good approximation for the steady limiting ray, $(x/t)_S = 0.7736$. In fact, any ray shown in the left half-plane of figure 15(*a*) for $Q = 0.0013$, including $(x/t)_T = 0.775$, is a good approximation for $(x/t)_S$, as they are all close in value. In contrast, $1 - We^{-1/2} = 0.7764$ is more than double $(x/t)_S = 0.3368$ for sinuous waves with $Q = 0.13$ (figure 16*a*). The merit of the extraction method is clearly seen in

https://doi.org/10.1017/jfm.2012.86 Published online by Cambridge University Press

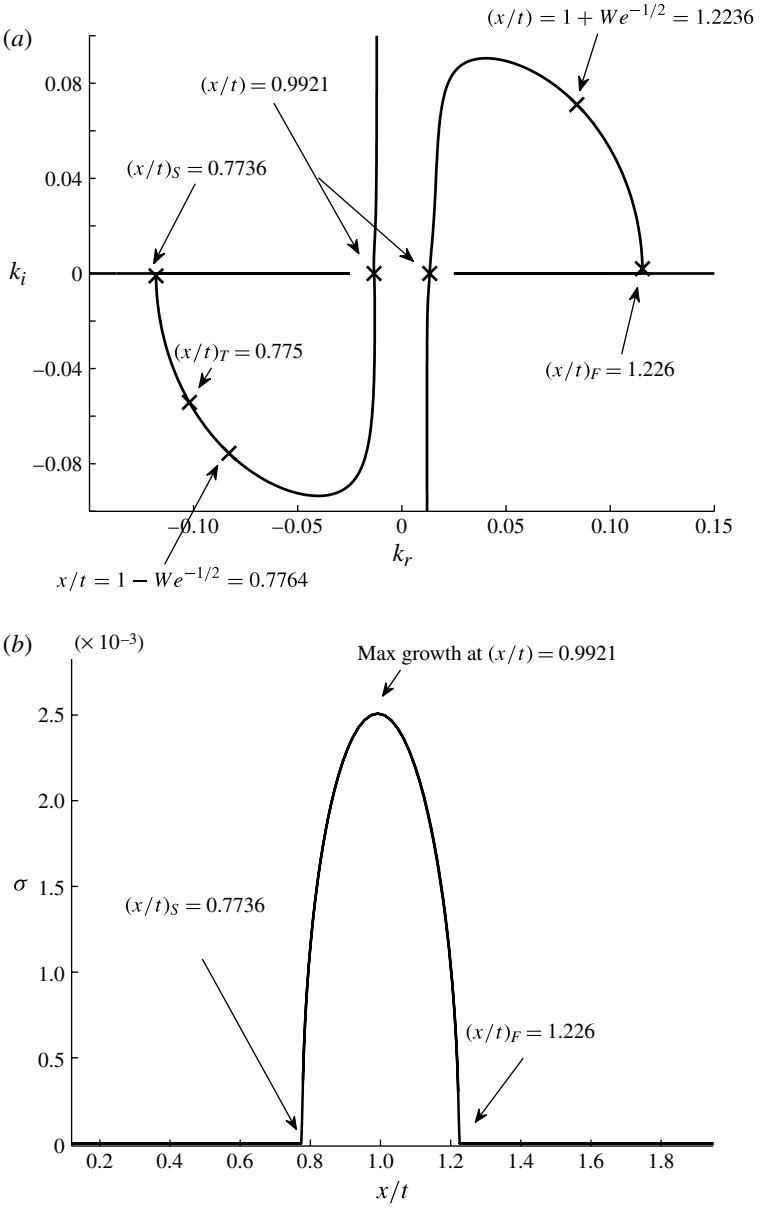



FIGURE 15. The $k_s$–$x/t$ distribution for sinuous waves with $We = 20$ and $Q = 0.0013$, determined from $D(k, \omega) = 0$ in (3.10). (*a*) Contours of $\mathrm{Im}(\partial\omega/\partial k) = 0$ indicate the locus of saddles. Relevant saddles ($\times$) are labelled with their $x/t$ value, shown here for one branch of $\omega(k)$. Here $(x/t)_S$ and $(x/t)_F$ are determined from the aggregate growth plot in (*b*); $(x/t)_T$ is determined by applying (2.20) to $D(k, \omega) = 0$ in (3.10) with $\omega_f = 0.2$.

figure 17 for varicose waves, where limiting ray values are clearly identified for a system that has no approximate characteristic velocities.

To validate these limiting rays, the series solution (3.13) is evaluated using an $\omega_f$ that permits spatial growth. The ray that tracks the front of the response, $(x/t)_F$, is validated in figures 18(*a*), 19(*a*) and 20(*a*), where the series solution is plotted for a

https://doi.org/10.1017/jfm.2012.86 Published online by Cambridge University Press

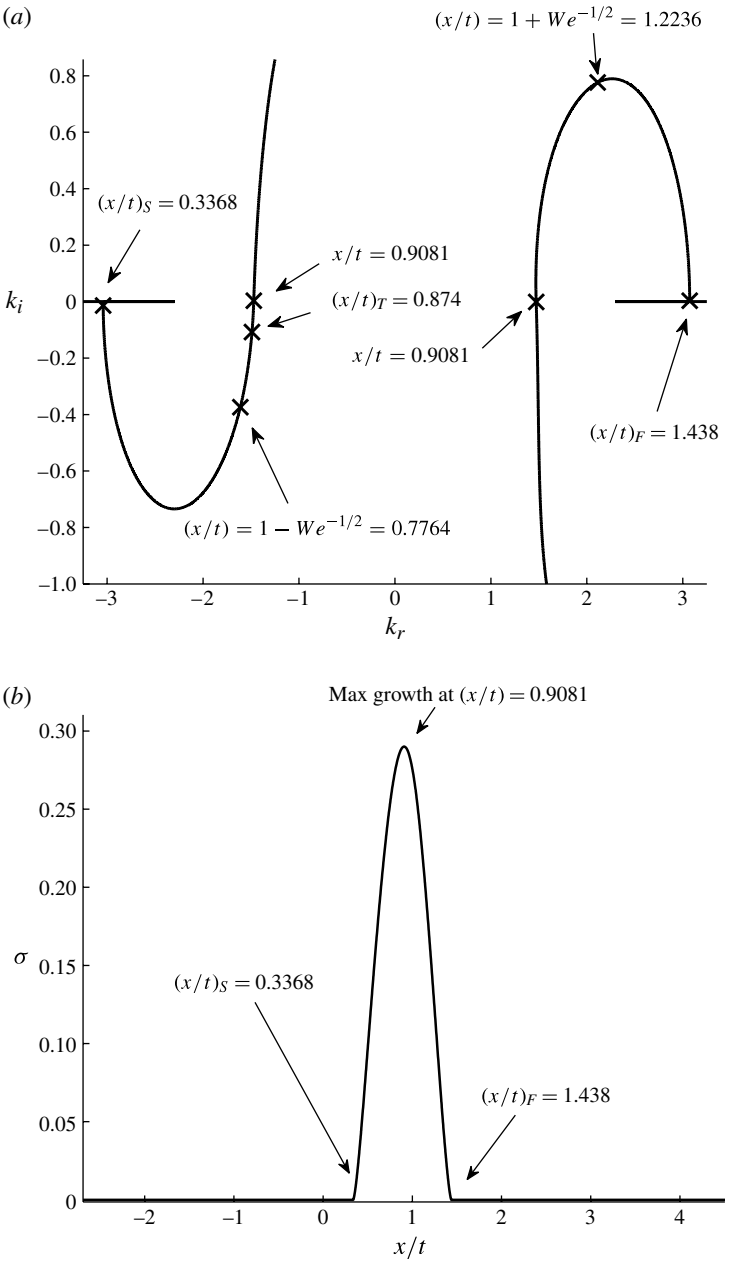



FIGURE 16. The $k_s$–$x/t$ distribution for sinuous waves with $We = 20$ and $Q = 0.13$, determined from $D(k, \omega) = 0$ in (3.10). (*a*) Contours of $\mathrm{Im}(\partial\omega/\partial k) = 0$ indicate the locus of saddles. Relevant saddles ($\times$) are labelled with their $x/t$ value, shown here for one branch of $\omega(k)$. Here $(x/t)_S$ and $(x/t)_F$ are determined from the aggregate growth plot in (*b*); $(x/t)_T$ is determined by applying (2.20) to $D(k, \omega) = 0$ in (3.10) with $\omega_f = 0.5$.

fixed time. The ray that tracks the extent of the steady spatially growing envelope, $(x/t)_S$, is validated in figures 18(*b*), 19(*b*) and 20(*b*), where the residue predictions ($\bullet$) are superimposed onto the series solution, identically matching for $0 < x/t < (x/t)_S$ in

https://doi.org/10.1017/jfm.2012.86 Published online by Cambridge University Press

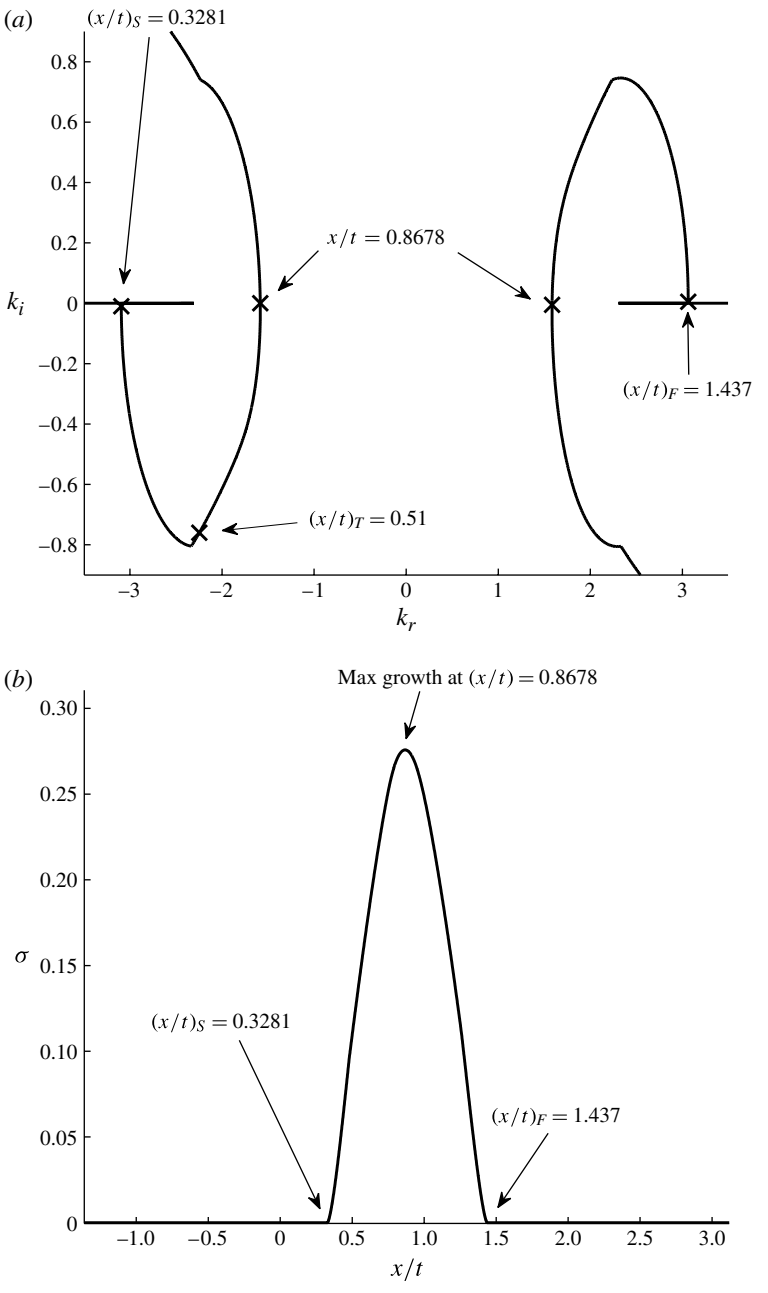



FIGURE 17. The $k_s$–$x/t$ distribution for varicose waves with $We = 20$ and $Q = 0.13$, determined from $D(k, \omega) = 0$ in (3.11). (*a*) Contours of $\mathrm{Im}(\partial\omega/\partial k) = 0$ indicate the locus of saddles. Relevant saddles ($\times$) are labelled with their $x/t$ value, shown here for one branch of $\omega(k)$. Here $(x/t)_S$ and $(x/t)_F$ are determined from the aggregate growth plot in (*b*); $(x/t)_T$ is determined by applying (2.20) to $D(k, \omega) = 0$ in (3.11) with $\omega_f = 1$.

each figure. The residue prediction is obtained using the leading-order contributions of (2.27), applied to (3.10) and (3.11). Note that no long-wavelength approximation

https://doi.org/10.1017/jfm.2012.86 Published online by Cambridge University Press

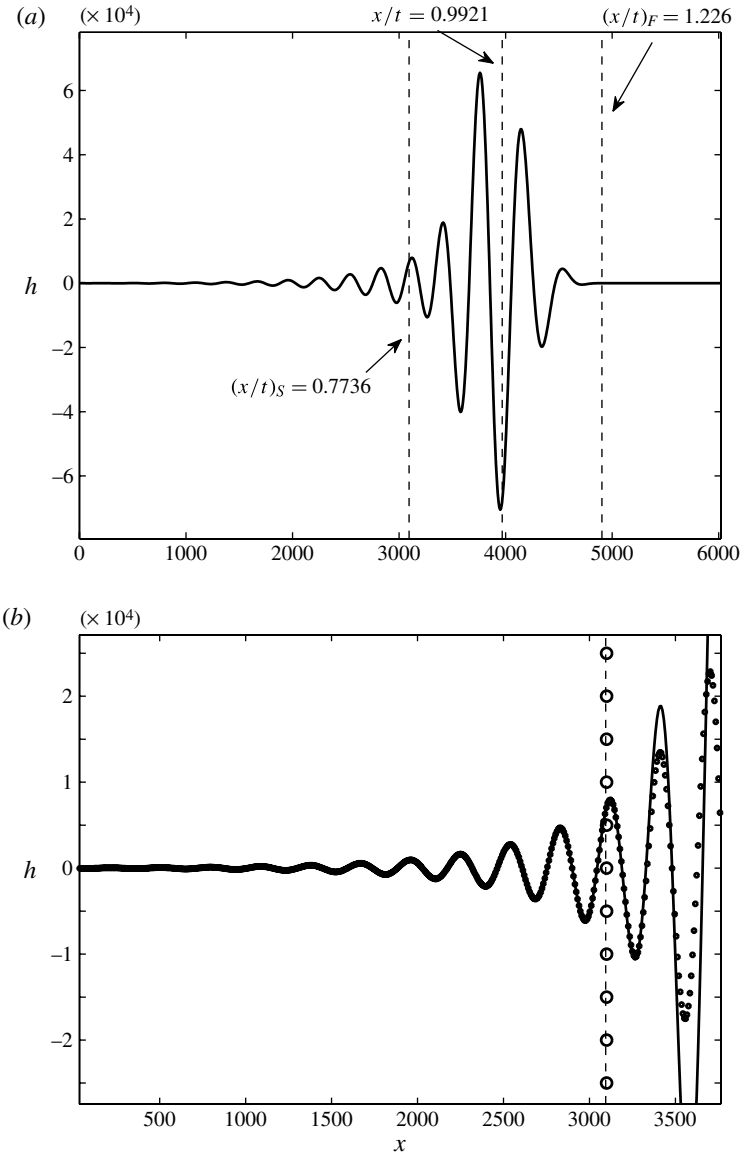



FIGURE 18. Series solution (3.13) of sinuous waves at $t = 4000$ with $We = 20$, $Q = 0.0013$, $\omega_f = 0.2$ and $A = 0.1$. The solution is constructed on a domain of length $L = 10\,000$ with $N = 400$. (*a*) Limiting rays shown as vertical dashed lines. (*b*) Magnification showing the steady spatial growth envelope. Here $(x/t)_T = 0.775$ (○) is slightly ahead of $(x/t)_S = 0.7736$ (dashed line). The series solution (——) exactly matches the residue prediction (●) for $0 < x/t < (x/t)_S$, given by (2.27) applied to (3.10).

is used when finding the $k_f = k(\omega_f)$ poles of (3.12). In order to calculate the residue prediction (2.27), a Newton–Raphson iteration is used to obtain the leading-order $k$-roots of (3.10) and (3.11).

For both sinuous and varicose waves, the rays $(x/t)_S$ and $(x/t)_F$ completely enclose the transient, shown in the series solutions plotted in figures 18(*a*), 19(*a*) and 20(*a*).

https://doi.org/10.1017/jfm.2012.86 Published online by Cambridge University Press

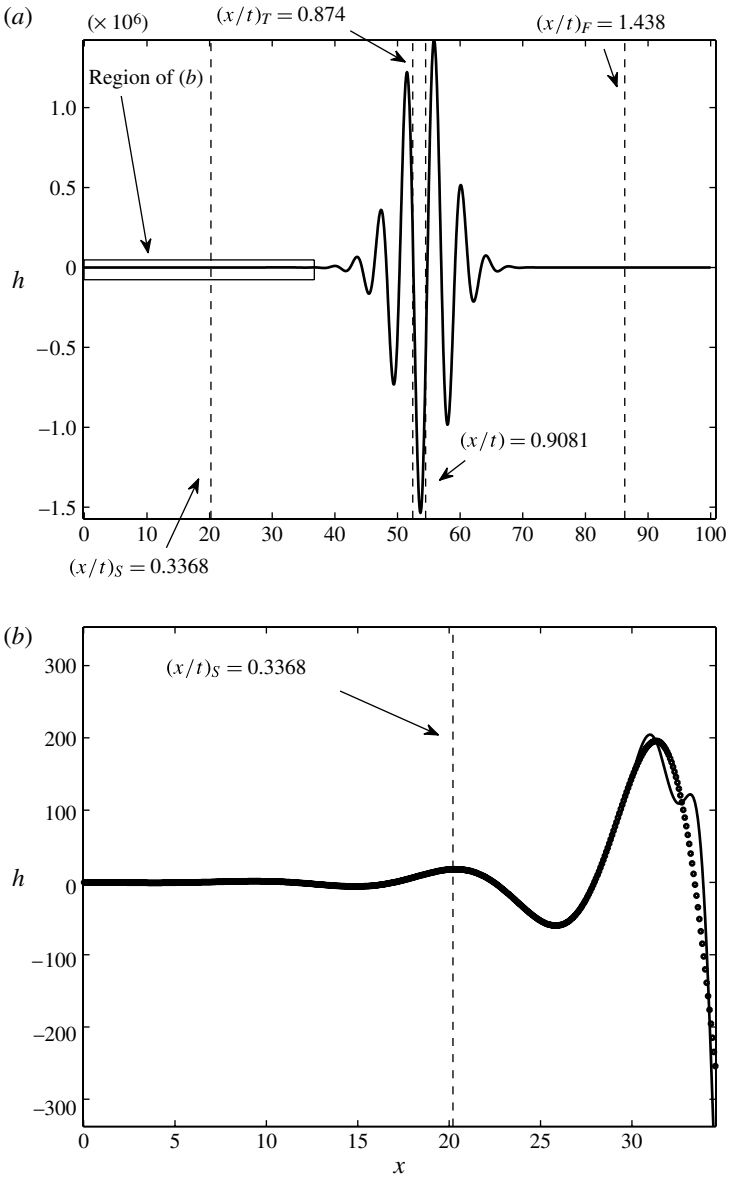



FIGURE 19. Series solution (3.13) of sinuous waves at $t = 60$ with $We = 20$, $Q = 0.13$, $\omega_f = 0.5$ and $A = 0.1$. The solution is constructed on a domain of length $L = 100$ with $N = 400$. (*a*) Limiting rays shown as vertical dashed lines. (*b*) Magnification showing the steady spatial growth envelope. The series solution (——) exactly matches the residue prediction (•) for $0 < x/t < (x/t)_S$, given by (2.27) applied to (3.10).

The magnified regions of these solutions in figures 18(*b*), 19(*b*) and 20(*b*) indicate that $(x/t)_S$ and $(x/t)_F$ conservatively bound the transient. As time increases, the wave packet solution associated with the transient will continually grow in width to fill the region between these two rays, since even small exponential growth, guaranteed to reside between these two rays, will eventually manifest itself.

https://doi.org/10.1017/jfm.2012.86 Published online by Cambridge University Press

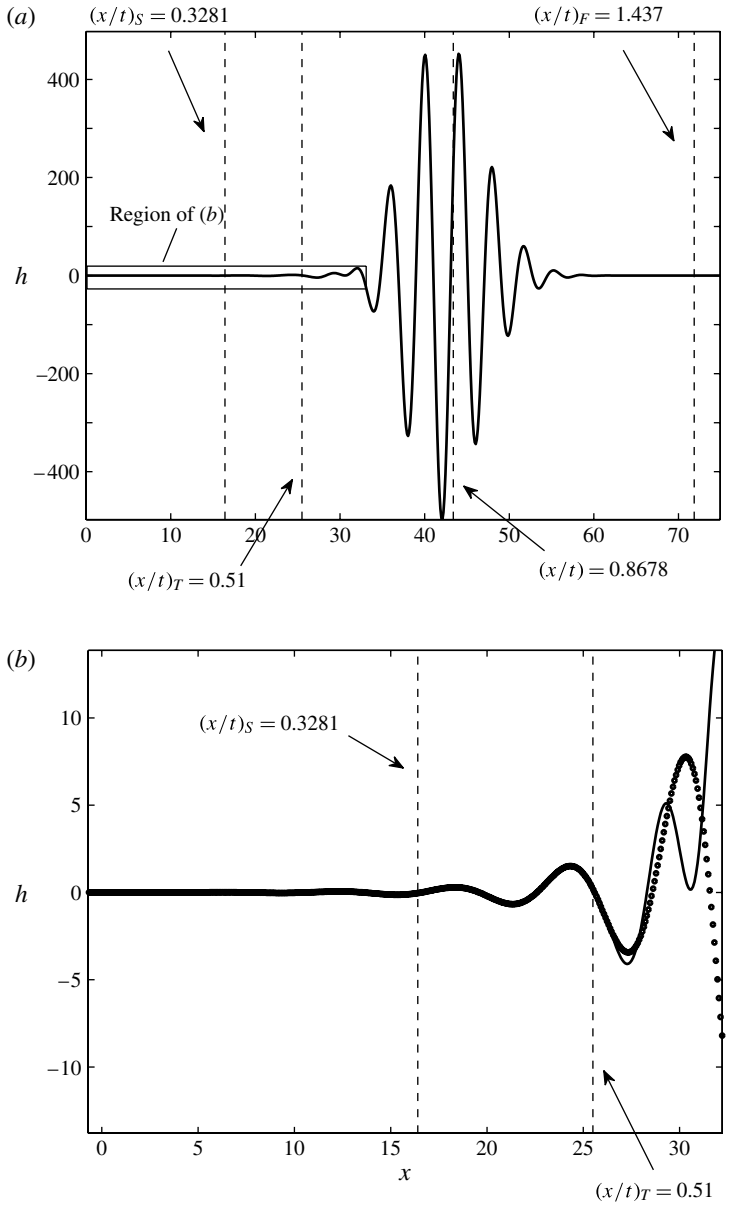



FIGURE 20. Series solution (3.13) of varicose waves at $t = 50$ with $We = 20$, $Q = 0.13$, $\omega_f = 1$ and $A = 0.001$. The solution is constructed on a domain of length $L = 75$ with $N = 200$. (*a*) Limiting rays shown as vertical dashed lines. (*b*) Magnification showing the steady-state spatially growing region. The series solution (——) exactly matches the residue prediction (•) for $0 < x/t < (x/t)_S$, given by (2.27) applied to (3.11).

## 4. Conclusions

The analysis provided here clearly demonstrates the subtleties involved in spatial–temporal stability analysis, particularly when studying an oscillatory-forced medium. Steady spatial growth in the signalling problem is intimately related to the

https://doi.org/10.1017/jfm.2012.86 Published online by Cambridge University Press

temporally growing transient response that precedes it. To witness spatial growth downstream (upstream), one must first force the medium at a frequency that permits negative (positive) imaginary wavenumbers, $k_f$, determined from the dispersion relation. In addition, one must be looking in a specific region, $x$, and at a specific time, $t$, such that the $x/t$ value corresponds with a saddle point of the Fourier integral solution. To actually observe spatial growth, this saddle must lie along a steepest descent path in the complex $k$-plane that encloses the pole $k_f$ with the real $k$-axis. As first identified by Gordillo & Pérez-Saborid (2002) and established in this paper, the correct integral responsible for spatial growth is necessarily the one which includes both a saddle point and the pole responsible for spatial growth, given here as $h_A$. This integral not only allows one to determine the growth rate, but also provides the $x/t$ rays that mark the transition between the spatially growing and temporally growing regions of the solution.

The approach provided in this paper provides a tractable method for obtaining practical information for convectively unstable flows that are continuously forced with oscillatory disturbances. Such flows are, in fact, controllable because the transient solution eventually propagates out of the domain. A spatially growing wave envelope that is bounded in time lags the transient and eventually fills the domain. In this work, we extract a closed-form transfer function that relates forcing amplitude and forcing frequency with the amplitude and frequency of the resultant spatially growing wave envelope. It is also important to determine the time at which the transient leaves the domain, as control of uniformity is lacking while waves grow freely in time. The precise $x/t$ value that determines the time $t$ at which the transient leaves the location $x$, can be determined from the dispersion relation, following the method provided in this work. In essence, we have combined the limiting ray technique of Gordillo & Pérez-Saborid (2002) with the established concepts found in Gaster (1968), Monkewitz (1990) and Huerre (2000) for identifying leading and trailing edge rays. The methodology developed here is shown to work for both a hyperbolic equation system (Klein–Gordon) as well as a non-hyperbolic dispersive system (liquid sheets); this is a demonstration of the generality of the procedure when saddles arise in the dispersion relation and govern the transient response. The spatial growth rate, wavelength and ultimately the phase of the steady spatially growing envelope are determined by the purely real forcing frequency through the dispersion relation. Although unstable flows are not desirable in processes that require flow uniformity, such as film coating, those that are convectively unstable may be controlled if disturbances to the system are process related and repetitive. Since the resultant spatially growing waves are bounded in time, it is possible to control the magnitude of these waves by controlling the magnitude of the offending disturbance.

## Acknowledgements

The authors would like to thank Professor D. S. Ross of Rochester Institute of Technology for useful mathematical discussions in support of this work. N.S.B. acknowledges partial support from NSF Award No. 1048579.

## Appendix A. Directions of steepest descent through convectively unstable saddles in the Klein–Gordon equation

For (2.1), the saddles associated with the convectively unstable transient are purely imaginary. The steepest paths away from these saddles are shown in figure 8 as an

https://doi.org/10.1017/jfm.2012.86 Published online by Cambridge University Press

ellipse and the $k_i$-axis. If we limit ourselves to a small region around the saddle, $k - k_s = |k - k_s|\mathrm{e}^{\mathrm{i}\theta}$, the steepest directions $\theta$ away from the saddle are $\theta = n\pi$ (ellipse) and $\theta = n\pi/2$ ($k_i$ axis), where $n$ is an integer. If we Taylor expand the exponential argument of (2.11) about the simple saddle $k_s$ and evaluate the denominator at $k = k_s$, we are then able to move the resultant coefficient of the exponential $f^{\pm}(k_s)$ outside of the integral, leading to

$$h_A^{\pm} \approx f^{\pm}(k_s) \int_{-\infty}^{\infty} \mathrm{e}^{\overbrace{-\mathrm{i}(\partial^2\omega^{\pm}/\partial k^2)|_{k_s}}^{-\gamma^2}\,(k-k_s)^2\,t}\,\mathrm{d}k \approx F^{\pm}(k_s) \int_{-\infty}^{\infty} \mathrm{e}^{-\gamma^2}\,\mathrm{d}\gamma \qquad (A\,1)$$

where the variable of integration has been transformed into $\gamma$ and $F^{\pm}(k_s) = f^{\pm}(k_s)/(\mathrm{d}\gamma/\mathrm{d}k)$. The path of steepest descent follows the specific directions $\theta$ that lead to $\mathrm{sgn}(\gamma^2) = +1$, guaranteeing convergence of (A 1). If we define

$$-\mathrm{i}\left.\frac{\partial^2\omega^{\pm}}{\partial k^2}\right|_{k_s} = \left|\left.\frac{\partial^2\omega}{\partial k^2}\right|_{k_s}\right| \mathrm{e}^{\mathrm{i}\alpha}, \qquad (A\,2)$$

then the condition that restricts (A 1) to be a path of steepest descent is

$$2\theta + \alpha = m\pi, \quad m \text{ odd} \qquad (A\,3)$$

which is an established result (Bleistein & Handelsman 1975). To determine which steepest path is that of descent for $h_A^+$ and $h_A^-$, one must first determine $\alpha$ from (A 2) and then evaluate (A 3) to obtain the correct $\theta$.

The branch cut between $k = -\sqrt{\mu}$ and $k = \sqrt{\mu}$ separates the complex $k$-plane into two Riemann surfaces, on which the integrands of $h_A^+$ and $h_A^-$ must be appropriately matched. In order to track the placement of $k_s$ on these surfaces (and by extension $\partial^2\omega/\partial k^2|_{k_s}$), it is useful to redefine the following quantity in polar form:

$$k_s^2 - \mu = \rho\mathrm{e}^{\mathrm{i}\pi + \mathrm{i}2r\pi}. \qquad (A\,4)$$

In (A 4), each integer $r$ represents a different Riemann surface, rotated $2r\pi$ about the branch line. By applying (A 4) to the definition of a saddle point,

$$\left.\frac{\partial\omega^{\pm}}{\partial k}\right|_{k_s} = U \pm k_s\,(k_s^2 - \mu)^{-1/2} = x/t \qquad (A\,5)$$

becomes

$$\pm\, k_s \rho^{-1/2}\, \mathrm{e}^{-\mathrm{i}\pi/2 - \mathrm{i}r\pi} = x/t - U. \qquad (A\,6)$$

The placement of saddles and choice of $+$ or $-$ can be determined from (2.13) and figure 6 (line ABC) for two ranges of $x/t$: $(x/t - U) > 0$ and $(x/t - U) < 0$. To ensure that the sign of $k_s$ in figure 6 remains consistent with the sign of $(x/t - U)$ in (A 6), the quantity $\rho^{-1/2}\,\mathrm{e}^{-\mathrm{i}\pi/2 - \mathrm{i}r\pi}$ must be negative imaginary, which leads to an even $r$ value. Evaluating (A 2) and using $r = 0$ gives

$$\begin{aligned} -\mathrm{i}\left.\frac{\partial^2\omega}{\partial k^2}\right|_{k_s} &= \frac{\mathrm{i}\mu}{(k_s^2 - \mu)^{3/2}} \\ &= \mathrm{i}\mu\rho^{-3/2}\,\mathrm{e}^{-\mathrm{i}3\pi/2} = \mu\rho^{-3/2}\mathrm{e}^{\mathrm{i}\alpha} \end{aligned} \qquad (A\,7)$$

which leads to $\alpha = \pi$ for saddles in both the lower and upper half-planes. Substituting this into (A 3) reveals that $\theta = n\pi$; thus, the ellipse is the path of steepest descent, leaving the $k_i$-axis as the path of steepest ascent.

https://doi.org/10.1017/jfm.2012.86 Published online by Cambridge University Press

## Appendix B. Integration through stable saddles of the Klein–Gordon equation

For (2.1), the temporally stable saddles that lag ($x/t < U - 1$) and lead ($U + 1 < x/t$) the transient are purely real valued. The convectively unstable saddles associated with the transient ($U - 1 < x/t < U + 1$) are purely imaginary. The transition between real and imaginary saddles occurs at two locations in the complex $k$-plane: for the rays $x/t = U + 1$ and $x/t = U - 1$, as shown in figure 6. For $h_A^+$, this transition occurs between $k_s = \mathrm{i}\infty$ and $k_s = \infty$ for $x/t = U + 1$ and between $k_s = -\mathrm{i}\infty$ and $k_s = -\infty$ for $x/t = U - 1$. For $h_A^-$, the transition occurs between $k_s = i\infty$ and $k_s = \infty$ for $x/t = U - 1$ and between $k_s = -\mathrm{i}\infty$ and $k_s = -\infty$ for $x/t = U + 1$. In § 2.2, the asymptotic behaviour of the integral solution for purely imaginary saddles ($U - 1 < x/t < U + 1$) is obtained by deforming the integration path along that of steepest descent, which is a semi-ellipse, given by the bracketed argument of (2.15). In the limits $x/t \to (U + 1)^-$ and $x/t \to (U - 1)^+$, this semi-ellipse approaches a semicircle of infinite radius. In § 2.2, we focus on the steepest descent paths associated with the purely imaginary saddles, as it captures the limiting rays that bound the transient. The real-valued saddles also contribute to the solution, and are necessary for capturing the behaviour associated with $x/t$ values that lead and lag the transient. In practice, we need to determine the steepest descent paths associated with these saddles to carefully examine their role. In this appendix, however, we focus on the limiting case of the infinite semicircular path, where the contributions of real-valued saddles may be elucidated easily and analytically.

To approach the rays $x/t = U \pm 1$ from outside of the transient region, we approach the infinite semicircle from either the saddles along the line ED or along the line FG, shown in figure 6 along the $k_r$-axis. To preserve the direction of this limit on the appropriate line of saddles, it is first useful to consider the following quantity in polar form:

$$k_s^2 - \mu = \rho \mathrm{e}^{\mathrm{i}\theta}. \tag{B 1}$$

### B.1. *Temporally stable behaviour of* $h_A^+$

For the integral $h_A^+$, given by the first term in (2.11), the real-valued saddles representing $x/t < U - 1$ are shown along the line ED in figure 6(*a*). A solution is constructed by closing the entire $k_r$-axis with a semicircular path, leading to

$$h_A^+|_{x/t\to(U-1)^-} = -\frac{A}{2\pi}\int_{C_{R\to\infty}} \frac{\mathrm{e}^{\mathrm{i}[kx-\omega^+(k)t]}}{-2\sqrt{k^2-\mu}[\omega^+(k)-\omega_f]}\,\mathrm{d}k + 2\pi\mathrm{i}\sum \text{ residues} \tag{B 2}$$

where $\int_{C_{R\to\infty}}$ is the infinite semicircle. The individual residues are multiplied by 1, $-1$ or 0, depending on whether a $k_f$ pole is enclosed by the infinite semicircle in the upper half-plane, enclosed in the lower half-plane or not enclosed at all, as indicated in figure 8. As the infinite semicircular path is approached, $\rho \to R \to \infty$ along the real axis in the left half-plane ($\theta = \pi$) as $x/t \to (U - 1)^-$. It follows that $\sqrt{k^2 - \mu} \to \sqrt{k^2} \to -k$ in (2.6), and (B 2) limits to

$$h_A^+|_{x/t\to(U-1)^-} = -\frac{A}{2\pi}\int_{C_{R\to\infty}} \frac{\mathrm{e}^{\mathrm{i}k[x/t-(U-1)]t}}{2k[\omega^+(k)-\omega_f]}\,\mathrm{d}k + 2\pi\mathrm{i}\sum \text{ residues}. \tag{B 3}$$

The path $\int_{C_{R\to\infty}}$ is valid for $x/t < U - 1$. It follows then, by Cauchy's integral theorem, that the contribution $\int_{C_{R\to\infty}}$ limits to zero in (B 3) if $k_i < 0$ and so the path is chosen

https://doi.org/10.1017/jfm.2012.86 Published online by Cambridge University Press

in the lower half-$k$-plane. This can be visualized in figure 9($a$) if the ellipse is replaced with an infinite semicircle, completely closing the path with the $k_r$-axis. For a given 'unstable' $\omega_f$ (i.e. $\omega_f^2 < |\mu(1-U^2)|$), a $k_{f1}$-type pole is enclosed, and (B 3) becomes

$$h_A^+|_{x/t\to(U-1)^-} = -\mathrm{i}A\frac{\mathrm{e}^{\mathrm{i}(k_{f1}(x/t)-\omega_f)t}}{\left[\dfrac{\partial D}{\partial\omega}\dfrac{\partial\omega}{\partial k}\right]_{k_{f1},\omega_f}}. \tag{B 4}$$

Note that (B 4) is exact for all time and not an approximation as $t\to\infty$. The cost of this approach is that (B 4) is exact only for $x/t\to(U-1)^-$ instead of the complete range $x/t < U-1$.

The real-valued saddles representing $U+1 < x/t$ are shown along the line FG in figure 6($a$). As the infinite semicircular path is approached, $\rho\to R\to\infty$ along the real axis in the right half-plane ($\theta=0$) as $x/t\to(U+1)^+$. It follows that $\sqrt{k^2-\mu}\to\sqrt{k^2}\to k$ in (2.6), and (B 2) limits to

$$h_A^+|_{x/t\to(U+1)^+} = -\frac{A}{2\pi}\int_{C_{R\to\infty}}\frac{\mathrm{e}^{\mathrm{i}k[x/t-(U+1)]t}}{2k[\omega^+(k)-\omega_f]}\,\mathrm{d}k + 2\pi\mathrm{i}\sum\text{ residues}. \tag{B 5}$$

The path $\int_{C_{R\to\infty}}$ is valid for $U+1 < x/t$. It follows, then, that the contribution $\int_{C_{R\to\infty}}$ limits to zero in (B 5) if $k_i > 0$ and so the path is chosen in the upper half-$k$-plane. This can be visualized in figure 9($c$) if the ellipse is replaced with an infinite semicircle, completely closing the path with the $k_r$-axis. For a given unstable $\omega_f$, no $k_f$ poles are enclosed and (B 5) reduces to $h_A^+|_{x/t\to(U+1)^+}=0$.

### B.2. *Temporally stable behaviour of* $h_A^-$

For the integral $h_A^-$, given by the second term in (2.11), the real-valued saddles representing $x/t < U-1$ are shown along the line FG in figure 6($b$). A solution is constructed by closing the entire $k_r$-axis with a semicircular path, leading to

$$h_A^-|_{x/t\to(U-1)^-} = -\frac{A}{2\pi}\int_{C_{R\to\infty}}\frac{\mathrm{e}^{\mathrm{i}[kx-\omega^-(k)t]}}{-2\sqrt{k^2-\mu}[\omega^-(k)-\omega_f]}\,\mathrm{d}k + 2\pi\mathrm{i}\sum\text{ residues}. \tag{B 6}$$

As the infinite semicircular path is approached, $\rho\to R\to\infty$ along the real axis in the right ($\theta=0$) half-plane as $x/t\to(U-1)^-$. It follows that $\sqrt{k^2-\mu}\to\sqrt{k^2}\to k$ in (2.6), and (B 6) limits to

$$h_A^-|_{x/t\to(U-1)^-} = -\frac{A}{2\pi}\int_{C_{R\to\infty}}\frac{\mathrm{e}^{\mathrm{i}k[x/t-(U-1)]t}}{2k[\omega^-(k)-\omega_f]}\,\mathrm{d}k + 2\pi\mathrm{i}\sum\text{ residues}. \tag{B 7}$$

The path $\int_{C_{R\to\infty}}$ is valid for $x/t < U-1$. It follows, then, that the contribution $\int_{C_{R\to\infty}}$ limits to zero in (B 5) if $k_i < 0$, and so the path is chosen in the lower half-$k$-plane. This can be visualized in figure 9($d$) if the ellipse is replaced with an infinite semicircle, completely closing the path with the $k_r$-axis. For a given unstable $\omega_f$, no $k_f$ poles are enclosed and (B 7) reduces to $h_A^-|_{x/t\to(U-1)^-}=0$.

The real-valued saddles representing $U+1 < x/t$ are shown along the line ED in figure 6($b$). As the infinite semicircular path is approached, $\rho\to R\to\infty$ along

https://doi.org/10.1017/jfm.2012.86 Published online by Cambridge University Press

the real axis in the left half-plane ($\theta = \pi$) as $x/t \to (U+1)^+$. It follows that $\sqrt{k^2-\mu} \to \sqrt{k^2} \to -k$ in (2.6), and (B 6) limits to

$$h_A^-|_{x/t\to(U+1)^+} = -\frac{A}{2\pi}\int_{C_{R\to\infty}} \frac{\mathrm{e}^{\mathrm{i}k[x/t-(U+1)]t}}{2k[\omega^-(k)-\omega_f]}\,\mathrm{d}k + 2\pi\mathrm{i}\sum \text{ residues}. \tag{B 8}$$

The path $\int_{C_{R\to\infty}}$ is valid for $U+1 < x/t$. It follows, then, that the contribution $\int_{C_{R\to\infty}}$ limits to zero in (B 8) if $k_i > 0$, and so the path is chosen in the upper half-$k$-plane. This can be visualized in figure 9(*b*) if the ellipse is replaced with an infinite semicircle, completely closing the path with the $k_r$-axis. For a given unstable $\omega_f$, a $k_{f2}$-type pole is enclosed and (B 8) becomes

$$h_A^-|_{x/t\to(U+1)^+} = \mathrm{i}A\frac{\mathrm{e}^{\mathrm{i}(k_{f2}(x/t)-\omega_f)t}}{\left[\dfrac{\partial D}{\partial\omega}\dfrac{\partial\omega}{\partial k}\right]_{k_{f2},\omega_f}}. \tag{B 9}$$

## REFERENCES


BARLOW, N. S., HELENBROOK, B. T. & LIN, S. P. 2011 Transience to instability in a liquid sheet. *J. Fluid Mech.* **666**, 358–390.

BARLOW, N. S., HELENBROOK, B. T., LIN, S. P. & WEINSTEIN, S. J. 2010 An interpretation of absolutely and convectively unstable waves using series solutions. *Wave Motion* **47**, 564–582.

BENDER, C. M. & ORSZAG, S. A. 1978 *Advanced Mathematical Methods for Scientists and Engineers I: Asymptotic Methods and Perturbation Theory*. McGraw-Hill.

BERS, A. 1983 Space–time evolution of plasma instabilities-absolute and convective. In *Handbook of Plasma Physics, vol. 1: Basic Plasma Physics 1* (ed. A. A. Galeev & R. Z. Sagdeev), pp. 451–517. North-Holland, ch. 3.2.

BLEISTEIN, N. 1984 *Mathematical Methods for Wave Phenomena*. Academic.

BLEISTEIN, N. & HANDELSMAN, R. A. 1975 *Asymptotic Expanions of Integrals*. Holt, Rinehart, and Winston.

CLARKE, A., WEINSTEIN, S. J., MOON, A. G. & SIMISTER, E. A. 1997 Time-dependent equations governing the shape of a two-dimensional liquid curtain. Part 2. Experiment. *Phys. Fluids* **9** (12), 3637–3644.

GASTER, M. 1968 Growth of disturbances in both space and time. *J. Fluid Mech.* **11** (4), 723–727.

GORDILLO, J. M. & PÉREZ-SABORID, M. 2002 Transient effects in the signaling problem. *Phys. Fluids* **14** (12), 4329–4343.

HUERRE, P. 1987 Spatio-temporal instabilities in closed and open flows. In *Instabilities and Non-equilibrium Structures* (ed. E. Tirapegui & D. Villarroel), vol. 1, pp. 141–177. D. Reidel.

HUERRE, P. 2000 Open shear flow instabilities. In *Perspectives in Fluid Dynamics* (ed. G. K. Batchelor, H. K. Moffatt & M. G. Worster). Cambridge University Press.

HUERRE, P. & MONKEWITZ, P. A. 1990 Local and global instabilities in spatially developing flows. *Annu. Rev. Fluid Mech.* **22**, 473–537.

LIGHTHILL, M. J. 1962 *Introduction to Fourier Analysis and Generalised Functions*. Cambridge University Press.

LIGHTHILL, M. J. 1978 *Waves in Fluids*. Cambridge University Press.

LIN, S. P. 2003 *Breakup of Liquid Sheets and Jets*. Cambridge University Press.

LIN, S. P. & JIANG, W. Y. 2003 Absolute and convective instability of a radially expanding liquid sheet. *Phys. Fluids* **15** (6), 1745–1754.

MONKEWITZ, P. A. 1990 The role of absolute and convective instability in predicting the behavior of fluid systems. *Eur. J. Mech. (*B/*Fluids*) **9** (5), 395–413.

MORSE, P. M. & FESHBACH, H. 1953 *Methods of Theoretical Physics*. McGraw-Hill Book Company.


https://doi.org/10.1017/jfm.2012.86 Published online by Cambridge University Press

RAYLEIGH, LORD 1896 *Theory of Sound*, vol. 2, 2nd edn. Macmillan and Co.

SQUIRE, H. B. 1953 Investigation of the instability of a moving liquid film. *Brit. J. Appl. Phys.* **4**, 167–169.

TAYLOR, G. I. 1959 The dynamics of thin sheets of fluid. Part II. Waves on fluid sheets. *Proc. R. Soc. Lond.* A **253**, 296–312.

WEINBERGER, H. F. 1965 *A First Course in Partial Differential Equations*. Xerox College.

WEINSTEIN, S. J., CLARKE, A., MOON, A. G. & SIMISTER, E. A. 1997 Time-dependent equations governing the shape of a two-dimensional liquid curtain. Part 1. Theory. *Phys. Fluids* **9** (12), 3625–3636.

WEINSTEIN, S. J. & RUSCHAK, K. J. 2004 Coating flows. *Annu. Rev. Fluid Mech.* **36** (29–53).

WHITHAM, G. B. 1974 *Linear and Nonlinear Waves*. Wiley-Interscience.

https://doi.org/10.1017/jfm.2012.86 Published online by Cambridge University Press